TPB evaporations and sensitivity plots for the DEAP-3600 dark matter detector

Talitha Bromwich

Candidate Number: 79409
MPhys Final Year Project 2013 to 2014
Supervisor: Dr Simon Peeters
University Of Sussex

Abstract

DEAP-3600 is a liquid argon WIMP dark matter direct detection experiment based at the SNOLAB underground laboratory in Canada. The detector utilises the organic crystalline solid tetraphenyl butadiene (TPB) to absorb the scintillated 128nm UV light generated by a WIMP-induced nuclear recoil in the liquid argon, and re-emit it as 440nm visible light. This project involved developing techniques for evaporating TPB of optimal thickness and smoothness on to acrylic slides to use in calibration development here at the University of Sussex. The topography of the TPB evaporated layers were analysed using an atomic force microscope. The deposits produced were on average $0.9\mu m$ thick, not varying by $0.15\mu m$ across the surface of the slide, well within the allowed variation parameters for the actual DEAP-3600 detector. This report also explores models for the WIMP-induced nuclear recoil energy spectrum for a target Argon mass, and the overall sensitivity of the DEAP-3600 experiment in a WIMP cross-section vs mass plot.

Preface

The results in section 3.1 were gathered by myself in the Invisibles Lab at Sussex under the direction of my supervisor Dr Simon Peeters. The analysis of the data is my own work. The calculations for the DEAP-3600 sensitivity plots in section 3.2 follow J.D. Lewin and RF Smith's *Review of mathematics, numerical factors, and corrections for dark matter experiments based on elastic nuclear recoil* [1]. The intermediate integrations in Appendices A and B are my own workings. The codes in Appendices C and D built on greatly simplified plots I generated previously as part of my summer research placement. The codes were written by me with assistance from Dr Peeters and codes by Professor Mark Boulay at Queen's University in Canada. The detector response function portion of the code was written by Professor Boulay.

Contents

1 Introduction

Dark Matter

Dark matter is currently one of the most intriguing puzzles in astro particle physics. The majority of the known mass in galaxies is contained in its stars and is luminous. You would therefore naturally assume that by looking up into space and counting everything luminous, we would arrive at a figure that would be broadly representative of the amount of mass in the universe. However, the behaviour of astronomical phenomena tells us there is significantly more gravitationally-interacting mass in the universe than we predict from a quantification of the amount of luminous mass we observe.

By significantly more mass, we in fact mean that these results are in radical disagreement. The latest results from the European Space Agency's Planck satellite measurements of the cosmic microwave background suggest we currently have no explanation for 84.5% of the mass contained in the universe [2]. This unexplained mass is given the placeholder name *dark matter*, as it does not appear to significantly absorb or emit electromagnetic radiation, only interacting very weakly, if at all, with ordinary matter. For this reason it is so far eluded detection, but we still see compelling evidence of it on a range of astrophysical scales.

1.1 Cosmological evidence for the existence of dark matter

The most direct evidence for the existence of dark matter comes from observations of the rotation curves of spiral galaxies. Because galaxies are constantly rotating, you can use the Doppler shift observed in the light emitted by stars at different places within the galaxy to calculate their velocities. You can then compare these velocities at different radial distances to plot the velocity distribution as you move further from the centre. We expect the velocity/radius relationship to adhere to equations derived from Newtonian gravity which equate centrifugal and gravitational forces giving

$$\frac{mv^2}{r} = \frac{GmM(r)}{r^2} \qquad \longrightarrow \qquad v = \sqrt{\frac{GM(r)}{r}}$$

where *M(r)* is the total mass contained within radius *r*. Because the majority of the luminous matter is located at the centre of spiral galaxies, we anticipate the velocity of stars should decrease as $\sim r^{-\frac{1}{2}}$ once you get outside the central bulge. *Figure 1* shows the results of observations gathered from the NGC 6503 spiral galaxy [3]. Instead of decreasing, the velocity distribution increases and then flattens out, remaining large well past the point where there is any visible mass. This suggests there must be a significant amount of non-luminous mass at larger galactic radii that we are not accounting for. Astrophysicists propose this missing mass is caused by a halo of effectively "invisible" matter that only interacts gravitationally with ordinary matter [4].

The rotation curve argument is very compelling evidence for the existence of dark matter but does not entirely rule out the possibility of some other baryonic matter that is simply dark. Planets, for example, are not luminous. Brown dwarf stars display very low luminosity because they are cool compared to other stars, and are therefore much more

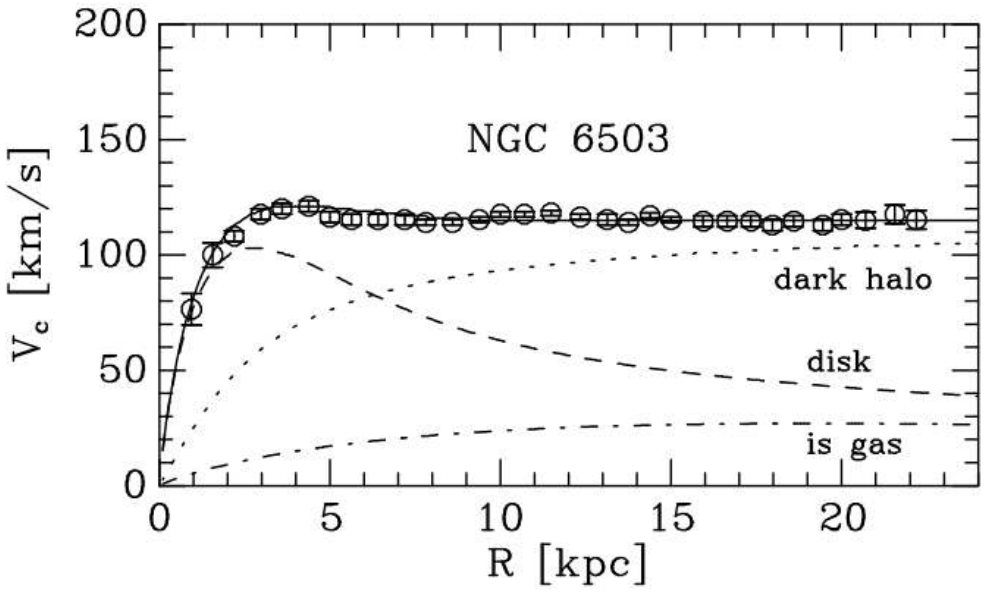

Figure 1: The observed velocities of objects orbiting the NGC 6503 galaxy as a function of their distance from the galactic centre. The dashed lines indicates contributions from the observable galactic disc and gas. The dotted line indicates the contribution hypothesised to be due to a dark matter halo. [3]

tricky to find. Another possibility is the stellar remnants of dead stars. However, none of these alternative mass sources are thought to exist in sufficient quantities to explain the extent of the deviation observed in the rotation curves [5], but even if they did, there are other astrophysical phenomena that indicate this missing mass cannot be explained by such objects.

On a larger scale, galaxies themselves are often gravitationally bound to each other and large baryonic gas clouds in groups known as clusters. The advantages of observing these much larger systems is that there are multiple ways of estimating the mass contained with them. These include gravitational lensing, where light coming towards us from more distant objects is distorted by the bending of space-time around closer massive galaxy clusters. These distant objects stretched, as if being viewed through a convex lens. The extent of this distortion can be used to derive information about the total mass and mass density distribution of the larger, closer mass causing the lensing. Observations, once again, suggest the presence of an excess of mass that is not visible [6].

Baryonic gas clouds are also strong X-ray emitters, and provide much more accurate representations of the ordinary mass content of galaxy clusters than visible light. From X-ray observations it is possible to infer the temperature of the gas, from which you can then determine the gas pressure and mass. The pressure outwards must match the gravitational pull inwards to enable stable cluster formation. However, gravitational attraction and pressure do not balance in clusters. This means there must be a large quantity of mass contained within galaxy clusters that does not contribute to the outward pressure (i.e. is non interacting), but does contribute to the gravitational attraction holding the cluster together.

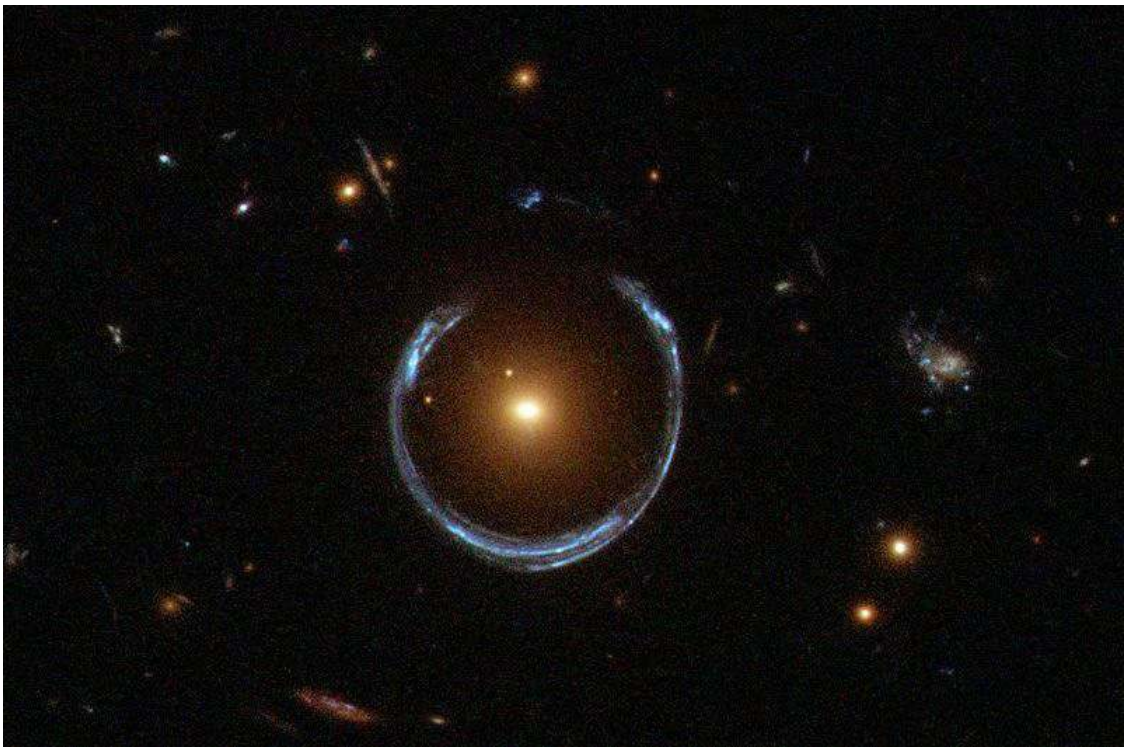

Figure 2: Gravitational lensing around LRG 3-757 resulting in a horse-shoe shaped Einstein Ring. Image credit: ESA/Hubble and NASA.

It is also possible to profile the velocity dispersion of the galaxies within the clusters, again using the Doppler shift, only in this case for entire galaxies as part of a larger cluster formation. This can then be used to determine the mass using the viral theorem, which equates the kinetic energy of a system with its potential energy. This method again displays a strong disparity with the mass estimated from the luminosity of a cluster. Additionally, because of the massive scale of clusters, they must have begun forming in the early stages of the universe. This means the ratio of baryons to dark matter contained within them should be roughly of the same order as the universe as a whole. Clusters thus provide excellent statistical representatives of the universal ratio of these various different types of mass, indicating that these mass discrepancies are a universe-wide problem.

The combination of all of these methods provides some of the best direct evidence for dark matter. The famous 1E 0657-56 galaxy cluster, known as the bullet cluster, is shown in *Figure 3* in an image which overlays the results from optical imaging (the individual galaxies in yellow) and X-ray observations emitted by baryonic gas (in pink). The gravitational lensing observed in the optical images of background galaxies is then used to determine the presence of dark matter (shown in blue). The bullet cluster is formed from two galaxy clusters that have collided into each other. The force of this galactic-scale impact has generated a shock front, with the two red gas clouds of the different clusters shaped into bullet-like trajectories. In contrast, the blue dark matter formations have passed through each other without interacting and retain their spherical halo-like shape.

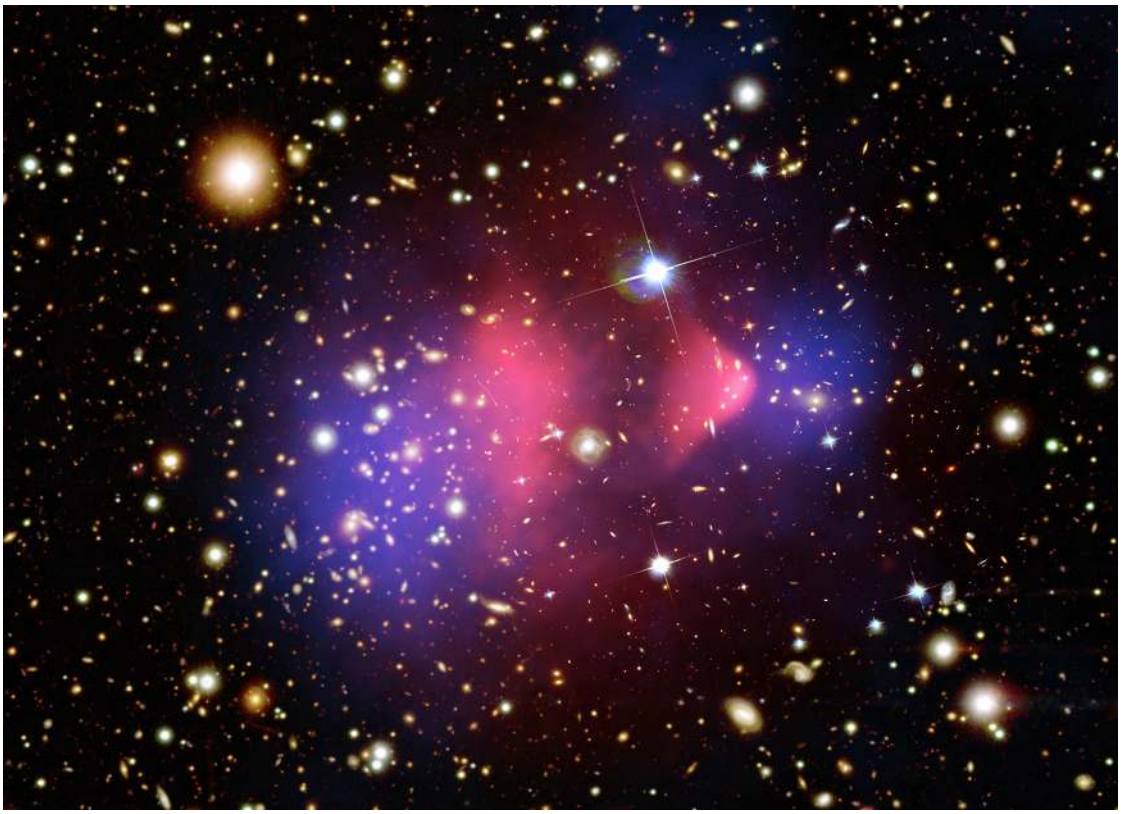

Figure 3: The Bullet Cluster 1E 0657-56 with three overlaid images. First the optical image of the galaxies, the x-ray observations of the baryonic gas clouds in pink, and the projected dark matter contents in blue, which has been inferred from gravitational lensing in background galaxies. Image credits: X-ray: NASA/CXC/CfA/ M.Markevitch et al.; Lensing Map: NASA/STScI; ESO WFI; Magellan/U.Arizona/ D.Clowe et al. Optical: NASA/STScI; Magellan/U.Arizona/D.Clowe et al.;

On an even larger cosmological scale, a large quantity of non-baryonic dark matter is required in the universe to satisfy the ΛCDM model, which encompasses our best understanding of the total energy-matter density composition of the universe and how it impacts the space-time geometry and requirements for early universe formation via inflation. The model is in significant agreement with experimental measurements of fluctuations in the cosmic microwave background, captured most recently by the Planck satellite, [2] and previously by the Cosmic Microwave Background Explorer (COBE) and Wilkinson Microwave Anisotropy Probe (WMAP).

These fluctuations in the cosmic microwave background result from adiabatic primordial perturbations in the early universe. Initially, in the very early inflationary period of the universe's conception, the perturbations in all the dark matter, baryons, neutrinos and photons were related to each other. But as the universe expanded, different particles were frozen out. Once they diluted sufficiently to fall out of causal contact with other types of particles, or with other particles of their own kind, their evolution ceased and over densities and under densities resulted in fluctuations which were locked in and simply stretched out over time. It is these frozen quantum fluctuations that we can see today on the relic cosmic microwave background. In this way, the particle content of the universe

is bound up in these massive cosmological radiation structures, and so from cosmological measurements we can set very tight constraints on the particle physics content of the universe.

Lighter particles, such as neutrinos, will retain relativistic speeds throughout expansion, and are referred to as hot particles. In contrast, much larger, cold particles will become non-relativistic much earlier, so their effect on the structure of the universe will be very different. These calculations are very involved, but they require the majority of the mass content of the universe to be cold and non-relativistic. Of course, as mentioned before, there is cold, non luminous baryonic matter in the universe in brown dwarf stars etc. But this is not not thought to be sufficient to explain the universe we have today. The ΛCDM model requires that the universe's energy-matter density is 26.8% dark matter and 4.9% ordinary matter. The remaining 68.3% is assigned to the equally mysterious dark energy, which causes the universe to expand at an accelerated rate.

The evidence for dark matter is very compelling, but so far its true nature remains a mystery. To date our best understanding of the fabric of our universe and the way it interacts is embodied in the standard model, which contains all the particles that makes up the matter we know of, and the force mediating bosons that dictates the way all these fundamental constituents interact with each other dynamically. However, there is currently no standard model particle candidate that fulfils the cosmological requirements of non-baryonic dark matter, so discovering whether or not dark matter is indeed a hitherto undetected kind of new particle, or something else more exotic, remains one of the greatest challenges of modern physics.

1.2 Theoretical particle physics candidates

Tantalisingly, although there is no standard model candidate for dark matter, there are lots of postulated theoretical candidates from physics beyond the standard model that fulfil all the required criteria. These candidates cannot interact electromagnetically, because dark matter is "dark", i.e. does not emit or absorb electromagnetic radiation, so will need to be electrically neutral. They will need a low velocity, as relativistic particles would not generate the observed cosmic microwave background spectrum [6]. They must also be effectively collisionless, as dark matter interacts negligibly with ordinary matter. It also needs to exist in sufficient quantities and be massive enough to explain the observed missing cosmological mass. All these things considered, any dark matter candidate needs to have a mass somewhere between $1GeV$ and $100TeV$, and an interaction cross section with ordinary matter of between 10^{-40} to $10^{-50}cm^2$ [8].

The first potential candidate for dark matter is the neutrino. The standard model neutrinos were at one time considered strong candidates for dark matter, being both neutral and only weakly interacting. However, as we learn more about them, we find their predicted relic density, relativistic speed and low upper limit on their masses make it impossible for them to make up the major component of the universe's missing dark matter [9]. The hypothesised heavy sterile neutrino however, is still neutral, but does not engage in either weak or the electromagnetic interactions, explaining why it could have hitherto not been detected. If such a particle exists, it would only interact via neutrino flavour mixing with the other "active" neutrinos. It has been calculated that

incoherent scattering production of sterile neutrinos in the early universe could result in candidates which meet all the cosmological constraints [10] for dark matter.

In the more exotic category, axions are a pseudo-Nambu-Goldstone boson which were originally derived as a solution to the problem of CP violation in QCD physics. However, they are also often considered potential dark matter candidates, as they would only interact via gravity and there are a number of proposed theories for how a large enough population could come to permeate the universe and account for the observed effects attributed to dark matter [11]. Kaluza-Kelin gauge boson particles from extra dimensional theories also provide viable candidates, falling within the allowed mass and relic density ranges [12].

However, the current favoured particle dark matter candidate is the weakly interacting massive particle, or WIMP, which arrises from theories of supersymmetry. The most promising of these is the lightest supersymmetric particle (LSP), known as the neutralino. It can be shown that the predicted relic abundance today of such a particle that only interacts on the weak scale with a cross section on the scale of $\sim pb$ would be exactly the required order of magnitude dictated by cosmological constraints [9]. Since the scale of the weak interaction has no obvious other connection to the critical density of the early universe, this coincidence is often called the WIMP miracle [13]. No supersymmetric particles have yet been discovered in detection experiments, but they currently offer the best means of modelling and understanding dark matter [5] and most dark matter detection techniques to date focus on WIMP-like candidates.

1.3 Dark matter detection

When it comes to attempting to detect WIMP dark matter and understand its properties, there are three main avenues of approach. The first option is to attempt to produce dark matter WIMPs in a particle accelerator. In the case of supersymmetric particles, such as the neutralino, these will escape the accelerator (much like neutrinos), leaving missing energy and transverse momentum from which their presence can be inferred. In indirect detection, you can look instead for the products of dark matter annihilation, as if neutralinos are Majorana particles, they will be annihilating with each other rapidly in dark matter dense regions of the universe. For this reason, cosmologists look to places such as the sun and the galactic centre for the gamma rays, neutrinos and antimatter predicted to emanate from regions of WIMP-WIMP annihilation.

The third possibility is direct detection of dark matter WIMPs here on Earth, which is the aim of the DEAP-3600 dark matter collaboration. The process of direct detection and the specifics as they relate to DEAP-3600 are discussed at length in the next section.

1.4 The principles of direct detection techniques

If WIMP dark matter exists throughout our galaxy then as the solar system rotates around the galactic centre, the Earth should be continually passing through an effective dark matter "rain" of particles. Because WIMP's are predicted to be very weakly interacting with normal matter, most of the time they will pass through us completely undetected. However, on rare occasions they could interact by colliding directly with the nuclei of ordinary matter, transferring some of their energy in the process. Therefore, in an extremely low background environment and with a sensitive enough means of detection, it should be possible to measure the recoil energy induced when WIMPs scatter off target nuclei. This is the principle of dark matter direct detection.

The type of detector required depends on the type of scattering process we assume for the WIMP-nucleon interaction. If the scattering is elastic, then the WIMP interacts with the entire target nucleus, generating a pure recoil. If the scattering is inelastic, then the WIMP interacts with the nucleons and some of the energy available for recoil is instead used to ionise or shift orbital electrons into an excited state, or to excite the nucleus into a higher energy state. The measured quantity for this type of scattering would be both the energy deposited in the nuclear recoil, and either the ionised electrons, or photons or phonons generated when the nucleons relax back to the ground state.

If the WIMP does interact with the nucleons, then there is the possibility for the couplings to be spin-dependent or spin-independent. In the former case, the cross section will be determined by the spin content of the nucleon J(J+1) [7]. However, in the later case where the coupling is spin-independent, the interaction cross section will become much greater with a larger number of nucleons. This means that the mass of the target nuclei determines which type of nucleon-WIMP scattering a detector is sensitive to, with spin-independent couplings dominating at large target masses.

Isolating the signals generated by WIMP scattering from the much more energetic and more frequent backgrounds is a huge challenge for direct detection experiments. Background sources include cosmic rays, and all forms of radioactive products in the detector surroundings, the materials the detector is made of and even the target material itself. WIMP detectors must therefore combine incredibly powerful background shielding and discrimination techniques to be sensitive enough to measure WIMP signals. To achieve this most detectors are housed deep underground where they are shielded from cosmic rays, and in ultra clean radio pure environments. The nuclear recoil energies transferred are typically expected to be in the range of 1 to $100keV$ [8] and the expected event rate no more than a few events per year. The energy threshold for measurements therefore needs to be very low, and the event rate maximised through large target masses and long exposure times.

Despite these huge challenges, there have already been many successes in the field, and there are currently more than 30 direct dark matter detectors operating or in development. The majority of these aim to measure scintillation light, phonons, ionisation electrons, or a combination thereof. The style of detection techniques can be broadly grouped into six main categories: solid scintillators measuring the photons (e.g. DAMA /

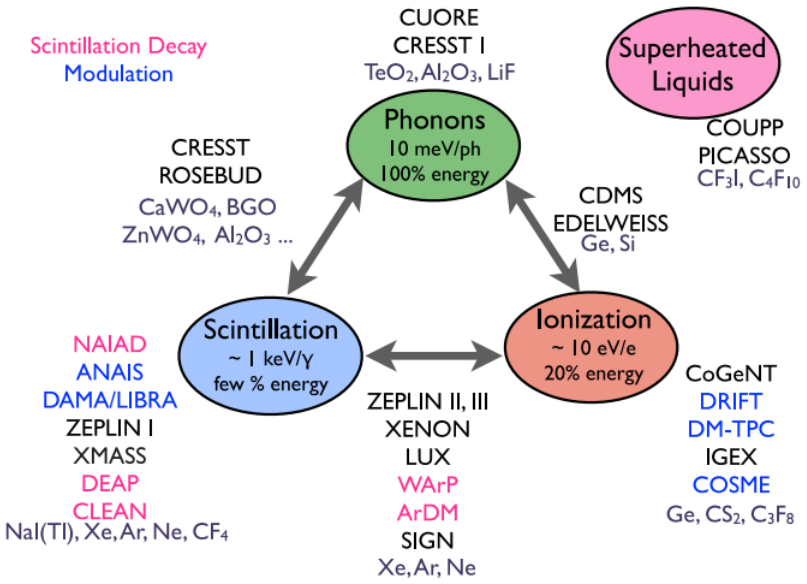

Figure 4: Energy deposition channels for WIMP detection experiments. Experiments are listed near the main readout channel, or between the two channels used. [14]

LIBRA); cryogenic semiconductor ionisation detectors (e.g. CoGeNT); cryogenic crystal ionisation and phonon detectors (e.g. EDELWEISS, CDMS, CRESST); superheated liquid bubble chambers (e.g. COUP, PICASSO); directional gaseous time projection chambers (e.g. DRIFT, DM-TPC); and liquid noble gas scintillation and ionisation detectors (e.g. DEAP, XENON100, LUX, XMASS, WArP).

This final type of liquid noble gas detection design has grown to dominate the dark matter direct detection field in recent years [6]. The noble elements make excellent target materials because the predicted event rate is relatively high, the scintillation or ionisation yield is quite large allowing detection at much lower energy thresholds, they are excellent at self-shielding against outside background sources, and they are transparent to their own scintillation light. The technology is also highly scalable and the targets fairly easily purified for reuse. Interactions with WIMPs in noble liquids also generate distinct scintillation pulses for nuclear recoil events electromagnetic recoil events, allowing for powerful background subtraction via pulse discrimination.

The current record for dark matter sensitivity detection is held by the Large Underground Xenon (LUX) experiment, with 90% confidence limits set on spin-independent WIMP nucleon elastic scattering with a minimum upper limit on the cross section of $7.6 \times 10^{-46} cm^2$ at a WIMP mass of $33 GeV c^{-2}$ [15]. There have been claims by the DAMA / LIBRA [16] and CoGeNT [17] groups, both reporting an observed annual modulation signal considered a so-called "smoking gun" for dark matter detection. However, these claims are controversial, mainly because the allowed mass-cross section parameter space has been ruled out by several subsequent experiments, including the LUX result. Now the race is on to probe deeper into the mass cross-section WIMP parameter space by lowering the available energy thresholds, increasing event rates and exposure times and continuing to improve background subtraction techniques. These are all things the DEAP-3600 direct detection experiment hopes to achieve in the coming years.

1.5 The DEAP-3600 detector

The DEAP-3600 direct dark matter detection experiment is a single phase 3600kg liquid argon scintillation light detector. That means it will be detecting just the photons of light generated by a WIMP-induced nuclear recoil in the target Argon, using pulse shape discrimination and background subtraction to isolate WIMP signals (see the next section for details on how this is achieved). It is currently in the process of being commissioned and will begin its first physics run in October 2014. A 3 year exposure time will allow for a $10^{-46} cm^2$ sensitivity to spin-independent scattering (see section 2.2 for the details of how this sensitivity is calculated), with a 15 keVee (60 keVr) threshold background limit, making it the new world leader for spin-independent WIMP measurements. It can be seen in the projected timescale plot below that the unique properties of argon, as compared to the xenon target of LUX, means DEAP-3600 will be more sensitive to all WIMP masses of around $100 GeV c^{-2}$ and above.

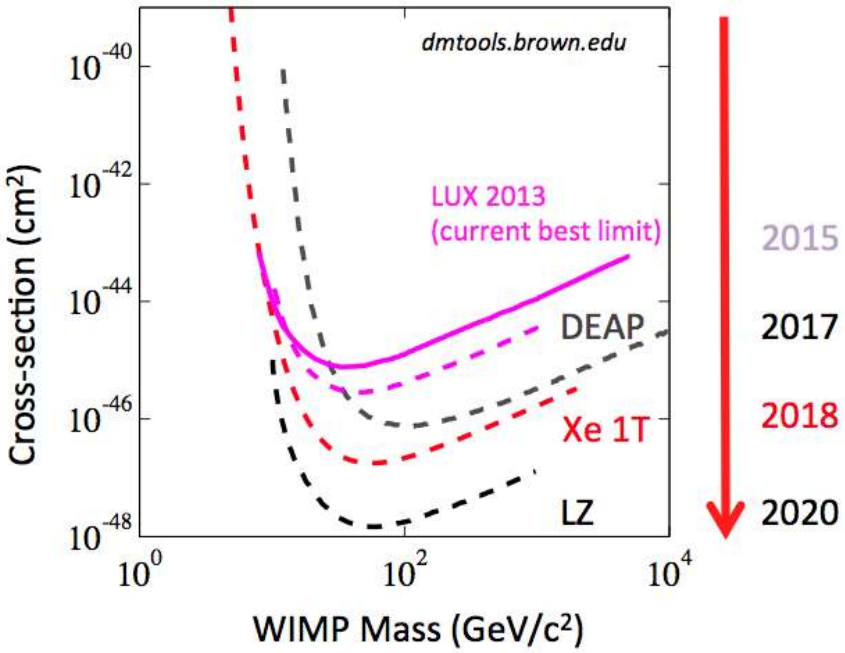

Figure 5: Timescale for the projected world's best spin independent measurements of the WIMP cross-section vs mass parameter space. [18]

The detector itself is composed of a large acrylic sphere that holds a target volume of 3600kg of cryogenic liquid argon. Surrounding the vessel are acrylic light guides, interspersed with filler blocks and insulation layers, leading to 255 8-inch Hamamatsu R5912 HQE PMTs all pointing inwards towards the central liquid argon. These PMTs have 75% coverage of the target volume, and a 32% quantum efficiency. The whole system is held in an outer steel shell, which is then submerged in an 8m diameter water tank. The neck of the detector carries the PMT cables, and cryogenic pump to cool and fill the detector with the liquid argon once sealed. The cryogenic equipment and data readout electronics systems are then housed on a deck above. A 3D rendering of the detector can be found below.

The experiment is housed in the SNOLAB Cube Hall, which is 6800 feet underground (6000 m.w.e.) in the purpose built scientific laboratory in the active Vale Creighton nickel mine near Sudbury, Ontario in Canada. All the materials used to build the detector were carefully monitored during construction and installation to minimise exposure to radon, and the radio pure acrylic vessel will be sanded to remove any radioactive impurities. The next stage in the commissioning process will be to evaporate the wavelength shifter tetraphenyl butadiene (TPB) on to the interior surface (see section 1.2.5) before the whole system is cooled and the liquid argon is pumped in through the neck of the detector to begin its physics run.

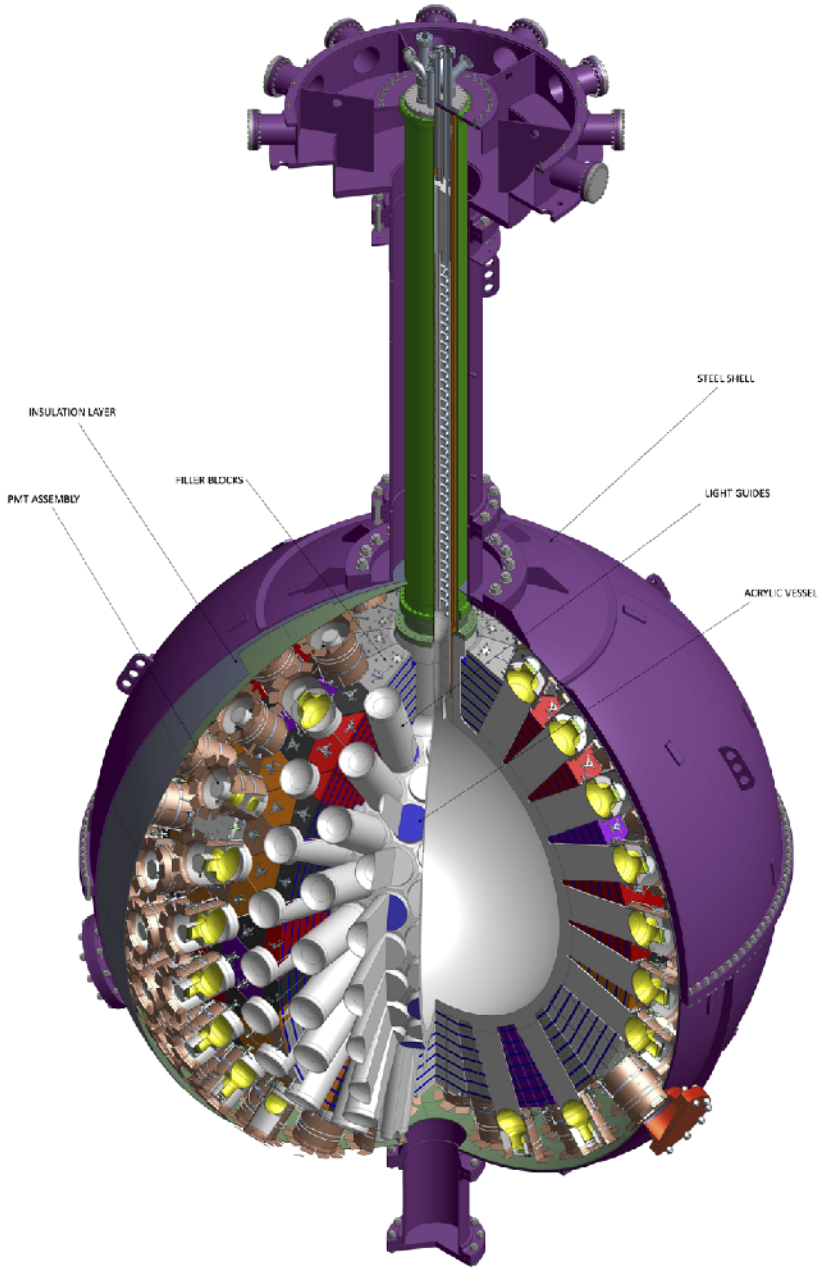

Figure 6: 3D rendering of the DEAP-3600 detector showing the acrylic vessel surrounded by light guides, acrylic filers and the 8" PMTs. Image courtesy of the DEAP-3600 collaboration.

1.6 Background subtraction in DEAP

Dark matter direct detectors are essentially very similar to radiation detectors, and thus any form of radiation that makes it into the active detector target volume can produce a signal that will either obscure or, more dangerously, look like a potential WIMP-induced signal. Background subtraction techniques must therefore combine a combination of active and passive shielding to reduce the overwhelming magnitude of radioactive decay and cosmic radiation backgrounds, and discrimination methods that differentiate any non WIMP signals that could bypass the shielding.

The first concern is cosmic radiation, which is composed of high energy protons and alpha particles from space which collide with the Earth's atmosphere, generating hadronic showers of mostly muons, pions and protons. All of these are a concern for DEAP-3600. To massively reduce the flux of cosmic rays or their secondary particle products reaching the detector or generating isotopes in the surrounding materials, the DEAP-3600 detector is housed underground at SNOLAB, and is thus very well shielded by the 2km of rock above it. This low beneath the Earth SNOLAB is able to reduce the high energy muon flux incident on the Earth's surface to just $0.27 m^{-2} day^{-1}$ [19].

To account for those remaining muons that do make it that far underground, the detector employs active shielding in the form of a muon veto water tank. Here PMTs are used to detect the Cherenkov light generated if muons pass through. Any measurable signal here is then used to veto coincident signals in the detector target volume. Because the likelihood of WIMP interactions is so rare, it is statistically highly improbable that they should interact in both the water tank and the detector volume.

The other major source of background is the radioactive decay of primordial isotopes contained in all naturally occurring materials, in particular radioactive ^{232}Th and ^{238}U, which have very long decay chains, and are emitters of gamma, alpha, beta and neutron radiation [20]. Of their many daughter isotopes, ^{222}Rn and ^{220}Rn are of particular concern, as although they decay quite rapidly, over a period of a few hours, they have the ability to move within and beyond the materials they form in. ^{222}Rn also decays to the isotope ^{210}Pb, which has a half life of 22 years, decaying to ^{210}Po which is an alpha emitter. Potassium ^{40}K is another important radioactive beta and gamma emitter that may be found in the PMT glass or surrounding rock.

To try and avoid the presence of these isotopes, all the materials used to construct the detector are as radio pure and to prevent the build up of ^{210}Pb on surfaces, everything is built in a radon-reduced lab area. Once completed, the components are regularly checked to monitor radioactive content. The inside of the acrylic vessel is sanded to remove a layer several microns thick before filling to remove any radon that could have formed on the interior surface [**?**]. Unfortunately the norite rock formation within which SNOLAB is situated provides the principle source of dust and radioactive backgrounds, and this cannot be removed or cleaned away. Norite rock contains 1.2% naturally occurring potassium, $1.2 ppm$ ^{238}U and $3.3 ppm$ ^{232}Th [19], providing a continuous flux of background radiation that has to be shielded or discriminated against.

The water shield muon veto will stop the majority of low energy neutrons and alphas, but the liquid argon target itself provides the primary and best means of shielding. Of the $3600 kg$ present in the core of the detector, only the central $1000 kg$ is used as a fiducial

volume from which data is gathered. The high atomic number and density combine in the active medium to produce excellent radiation stopping power [21]. For those that do make it through to the central fiducial volume, event position reconstruction using the PMT calibration enables the isolation of alpha and neutron scintillation signals that will tend to be nearer the outside of the detector and will leave a clear track, whereas a WIMP would only interact once and is uniformly likely throughout the detector.

The remaining sources of background are gamma and beta radiation events entering from outside, and radioactive ^{39}Ar, which is a strong beta emitter with a half life of 269 years. ^{39}Ar is cosmogenically generated and makes up 8×10^{-16} grams per gram of natural argon [22], amounting to 3.3×10^{7} decays per kg per year [23]. One way to reduce the impact of this background is to use depleted sources of argon from underground reservoirs. Being underground for extended periods means most of the ^{39}Ar will have decayed away, and lack of exposure to the atmosphere means there will have been no further cosmogenic radioactive isotope production.

However, even with depleted sources and all the shielding mentioned, there is still the problem of isolating WIMP-induced recoil events from the electromagnetic recoil events caused by gamma and beta radiation. This is where the nature of argon scintillation and pulse shape discrimination techniques becomes vital to the success of DEAP-3600.

1.7 Argon scintillation and pulse-shape discrimination

Argon has a distinct scintillation process that involves the production of diatomic excited molecules (or excimers), which are very beneficial for WIMP dark matter direct detection. The scintillation pathways result in a very large photon yield per excitation event and stable argon atoms cannot be re-excited by the scintillation light generated by the excimers, so no signal strength is lost to reabsorption. But most crucially, the pulse shapes produced by the dimer scintillation also enables the discrimination between scintillation caused by nuclear recoil (such as collision with a WIMP or a neutron), and electromagnetic recoil (with beta or gamma decay).

There are two distinct ways argon can form excimers: excitation and ionization. The first involves the formation of an electronically excited state denoted Ar^*, and the second the formation of ions, denoted Ar^+, which then bond with neighbouring argon atoms in the ground state. The processes are quite distinct but both ultimately involve the production of the same excited diatomic molecule, Ar_2^*, which relax to the ground state via the emission of 128nm VUV radiation in the final stage. The details of the two different processes are

$$Ar^* + Ar + Ar \rightarrow Ar_2^* + Ar$$

$$Ar_2^* \rightarrow 2Ar + h\nu$$

for excitation and

$$Ar^+ + Ar \rightarrow Ar_2^+$$

$$Ar_2^+ + e^- \rightarrow Ar^{**} + Ar$$

$$Ar^{**} \rightarrow Ar^* + \text{heat}$$

$$Ar^* + Ar + Ar \rightarrow Ar_2^* + Ar$$
$$Ar_2^* \rightarrow 2Ar + h\nu$$

for ionisation, where $h\nu$ denotes the VUV photon and the step resulting in the production of heat denotes a non-radiative transition [24].

The final scintillation step can involve a transition from one of the two lowest electronic excited states, the triplet state $^3\Sigma_u^+$ or the singlet state $^1\Sigma_u^+$, to the ground state $^1?\Sigma+_g$ [21]. The names singlet and triplet denote the nature of the pairing of the spin of the excited electron with an unpaired electron in the dimer molecule [6]. Both transitions produce an identical wavelength photon however, they have very different decay lifetimes because the transition from the triplet state is forbidden, involving a spin flip. It becomes possible through a spin-orbit coupling [25], but survives $\sim 1.5\mu s$ in argon, compared to the singlet which decays in $\sim 7ns$.

This difference in lifetime allows for pulse shape discrimination in DEAP-3600 because different types of excitation result in different ratios of triplet to singlet excimer formation. Nuclear recoils have been shown to produce a smaller number of triplet-state excimers compared to electromagnetic gamma or beta excitations [25]. Consequently the pulse shape detected in the PMTs from electromagnetic recoil will have more light later on in the pulse from the relaxation of a greater number of triplet state excimers. In contrast, nuclear recoil pulses will be more concentrated at the beginning of the pulse. In addition nuclear recoils also tend to produce less total light than electronic recoils [6].

DEAP-3600 uses a parameter called f_p, known as f-promt or the prompt fraction, which denotes the fraction of light detected from an event in the detector across a window of approximately $90ns$. The plot below shows this fraction in the first 90s as a function of energy for nuclear and electronic recoils. This distinct difference in energy patterns allows for powerful pulse shape discrimination that can separate all gamma or beta-induced events in the detector from nuclear recoil events, caused by WIMPs.

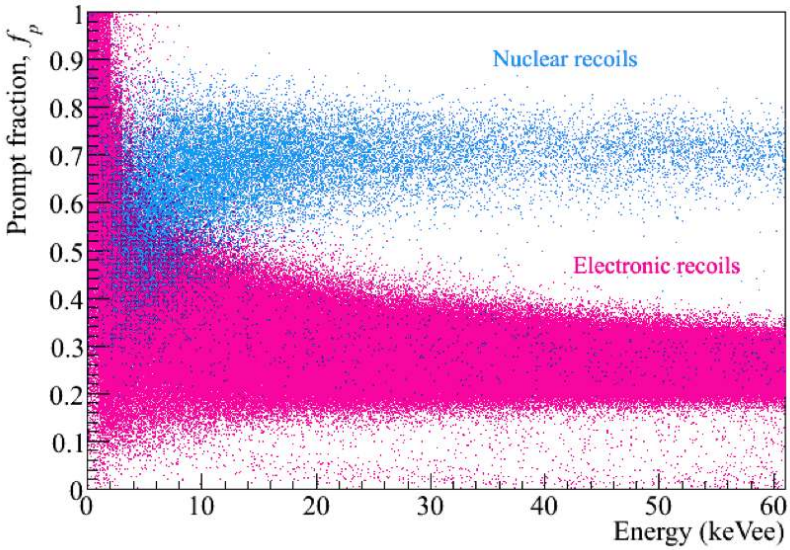

Figure 7: The pulse shape discrimination between nuclear recoils and electronic recoils, where prompt fraction denotes the fraction of light detected in the first 90s of a pulse [6].

1.8 TPB wavelength shifting

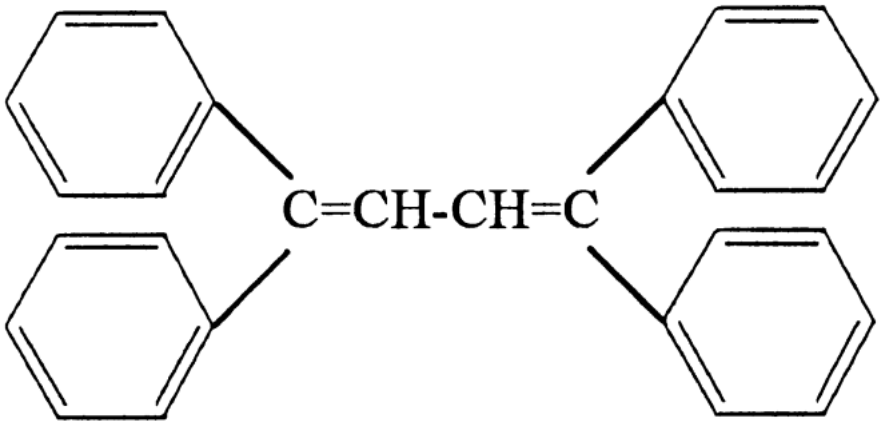

Figure 8: 1,1,4,4-Tetraphenyl-1,3-butadiene (TPB), $(C_6H_5)_2C{=}CHCH{=}C(C_6H_5)_2$ molecular structure with four benzene rings on each corner [26].

The wavelength of the nuclear recoil-induced scintillation light generated in argon has a peak wavelength of $128nm$, which falls in the vacuum ultra violet spectrum. Argon, as mentioned in the previous section, is transparent to its own scintillation light, so the photons are able to pass through the target volume without being reabsorbed. However, light of this spectral region is strongly absorbed by air, acrylic or glass mediums, making most photomultiplier tube (PMT) technologies ineffective for detection. To get around this issue, wavelength shifters can be deposited on the interior surface of detectors to down-scatter the photons into the visible range, so they can then propagate freely through acrylic light guides into PMTs to be detected. In DEAP-3600, the organic crystalline solid 1,1,4,4-Tetraphenyl-1,3-butadiene (TPB), $(C_6H_5)_2C{=}CHCH{=}C(C_6H_5)_2$, is used to accomplish this.

The wave shifting process is due to the photochemical phenomena of photoluminescence, or more specifically in the case of TPB, fluorescence. This occurs when a molecule's electrons are excited to higher energy states by an input of energy from absorbed electromagnetic radiation. The electron then rapidly relaxes to the ground state, releasing the excess energy as a photon of a specific frequency corresponding to the size of the energy drop. In fluorescence, this process occurs on nanosecond timescales, with the electron in question excited to the S_1 state, and relaxing to the S_0 state [27].

Many different kinds of molecules are capable of being excited to higher vibrational states, and in this way and may exhibit varying degrees of very weak fluorescence, but only specific kinds of molecules are capable of the amount of florescence required to be used as an efficient wavelength shifter. The most intensely fluorescing molecules usually contain conjugated systems of connected p-orbitals with alternating single and double bonds [28]. This formation produces delocalised electrons, known as π electrons, within the molecule structure. The most recognisable example of this phenomena is in benzene rings, of which TPB has four.

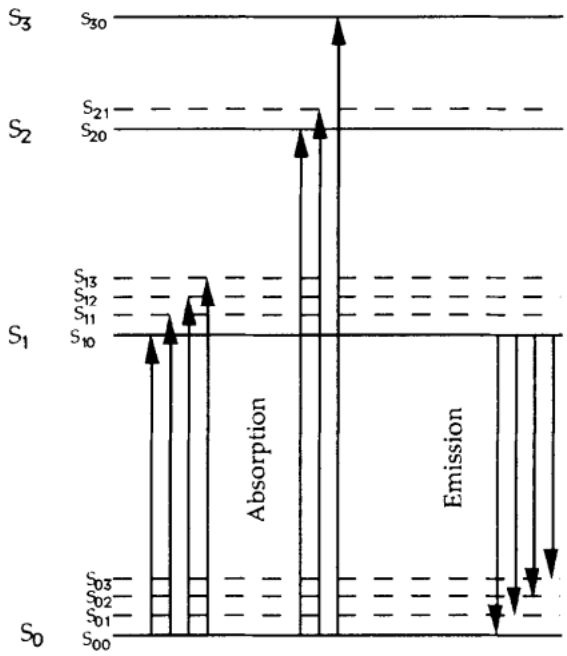

Figure 9: Energy levels of an organic molecule with π-electron structure. [27]

These "free" electrons can be treated like the electrons of metals and semiconductors, and the available energy level transitions can therefore be very well predicted. The figure above shows the typical energy levels of a photoluminescent molecule like TPB with π electron configurations. However, the exact energy spectrum of the emitted and absorbed radiation is dependent on the conformation and symmetry of the specific molecule [29]. For example, when the π-electron system is more dispersed across the molecule, the transition energy becomes smaller.

To be used as a wave shifter, fluorescent materials must also, obviously, absorb and emit at different wavelengths. In the majority of cases fluorescent molecules radiate photons that are of a lower energy than the photons that were originally absorbed. This is because the excited electron will rapidly shed excess vibrational energy through collisions with nearby molecules to fall to the lowest possible level of S_1 before fluorescence occurs. This fraction of energy lost from the excitation energy available for fluorescence, is known as Stokes Loss. It is caused by the change in the equilibrium configuration of the molecule during absorption, and by the frequency at which the transition occurs [29].

TPB has one of the highest fluorescent efficiencies of all known wavelength shifters for 128nm light [30] and can be easily evaporated on to surfaces, where it forms an adherent and durable layer. The visible light TPB then emits has a peak wavelength of $440nm$, with a spectrum ranging from 390 to $529nm$ [31], which falls directly within the peak radiant sensitivity and quantum efficiency region of Hamamatsu's 8-inch R5912 HQE PMTs [32]. The decay time of the wave shifting process in TPB takes approximately $1.68ns$ [33], so it does not interfere with the pulse shape discrimination in DEAP-3600. Crucially, it has also been shown that TPB is incredibly efficient in the wave shifting process [31], so you do not loose energy resolution.

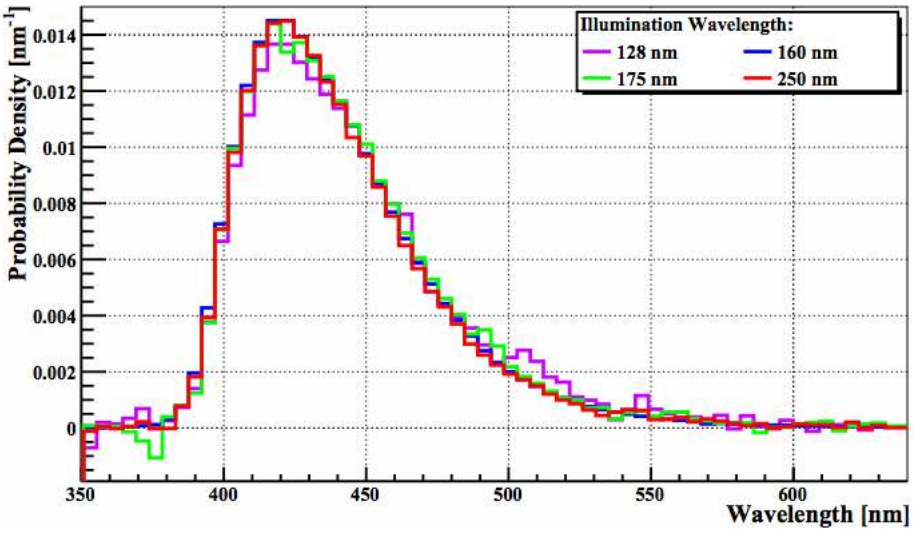

Figure 10: Visible re-emission spectrum for a TPB film illuminated with 128, 160, 175, and 250 nm light. All spectra are normalised to unit area. Plot from Gehman V.M. et al. Fluorescence efficiency and visible re-emission spectrum of tetraphenyl-butadiene films at extreme ultraviolet wavelengths [31].

For all these reasons, TPB makes an excellent wave shifting candidate for the DEAP-3600 experiment, and techniques have been developed at SNOLAB to evaporate it across the entire interior surface of the detector before it is filled with liquid argon [23]. In order to test optical calibration equipment for the detector here at the University of Sussex, it is necessary to replicate these conditions on a smaller scale. This means evaporating TPB of identical thickness and smoothness on to small acrylic slides.

The literature suggestions for optimum TPB thickness range from 0.07 (for 185nm light) [34] to 0.2mg/cm^2 (for 58nm light) [35], falling by approximately 10% when shifting 0.03mg/cm^2 either side. Experiments with light yield efficiency with DEAP-1 have concluded that the TPB layer for DEAP-3600 should aim to be on average 0.1 mg/cm^2 (or $0.9\mu m$) thick, not varying by more than 30% across the interior surface [23]. The aim of this project is to produce TPB slides that fulfill these criteria.

TPB has a low boiling point of around $207 - 209°C$ $(480 - 482K)$ [36] and goes through a liquid phase when it evaporates, rather than sublimating. This means if heating occurs too quickly there can be bubbling, leading to an uneven coating [27]. It is therefore very important that the heating process is slow and well controlled throughout evaporation to generate a uniform coating and meet the experimental parameters required.

It has been observed that TPB degrades when exposed to common fluorescent lights and ambient sunlight in laboratories, losing efficiency [37] and visibly changing colour from white to yellow [38] with prolonged exposure. So it is important the TPB is always stored in a sealed, dark environment when not being used. TPB may cause skin and respiratory irritation, so gloves should be worn when handling it and dust generation and accumulation should be minimised.

2 TPB evaporations

2.1 Objectives for the evaporation

The TPB slides will be used to test optical calibration equipment for the DEAP-3600 detector so need to be of identical thickness and smoothness as those proposed for DEAP. The requirements of the slides are:

- The TPB layer must be on average $0.9\mu m$ thick.
- The thickness must not vary by more than 30% across the surface of the slide, so no more than $0.3\mu m$ variation.
- On a microscopic scale, the thickness variation should be minimised.
- The TPB covering must not have any holes or areas without TPB coating.
- The TPB layer must adhere well to the acrylic surface.
- The acrylic slides must fit in standard optical mounts used for testing the calibration equipment.

In DEAP-3600 the TPB layer will be produced using a spherical crucible with optimised TPB exit holes arranged across its surface [23]. The TPB will be placed inside and the crucible will be lowered through the neck of the detector to the centre of the acrylic sphere and slowly heated by a heating wire wrapped around it. The TPB will then evaporate out radially to produce a uniform layer across the interior surface of the detector. The objective of this experiment was to replicate this process as closely as possible by evaporating samples of TPB up on to small acrylic slides in an evaporator.

2.2 Vacuum requirements

To produce a smooth, even coating of TPB it is vital the molecules follow a straight path upwards from the crucible on to the slide when they evaporate. Excessive collisions with air molecules or other impurities may compromise the integrity of the resulting deposit. This means working at low pressures in a vacuum to remove air molecules that might collide with the TPB and disturb its path.

The equipment available for vacuum generation and evaporation in the Invisible Labs at Sussex is an Edwards oil vapour diffusion pump. This incorporates a glass vacuum enclosing bell jar, heating elements, and a standard two pump roughing and backing configuration. The glass dome is placed over the evaporation area and twisted to form a seal with the metallic surface. The roughing pump is then switched on and used to bring the pressure down to around $10^{-1}Torr$. Then a lever connecting the evaporation area to the diffusion pump is opened and the pump is turned on.

The diffusion pump contains an electric heater which generates a vapour from the pump oil. The roughing is used first, as this vapour generation process requires an initial reduced pressure. Once the vapour is formed it is forced up through the diffusion pump jet channels. The outside of the pump is then cooled by running water, which causes the oil vapour to condense and run back down. Air and other molecules that enter the

pump encounter these vapour molecules and collide with them. The momentum transfer from these collisions causes the air molecules to be moved down through the pump in the direction of the cooling vapour, and evacuated by a mechanical backing pump. An ion gauge is then used to monitor the pressure inside the evacuated bell jar.

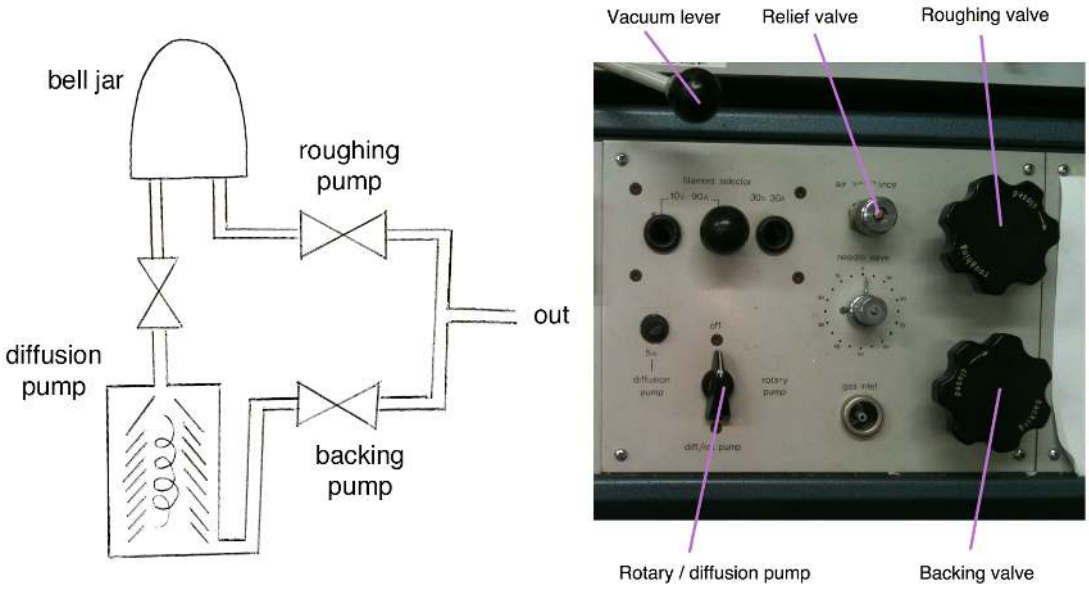

Figure 11: The diffusion pump basic layout and controls. There is an additional connector which runs cold water in and around the diffusion pump.

TPB is a large molecule with a complex geometry, so its mean free path can only be approximated. TPB's evaporation temperature is between $207 - 209°C$ $(480 - 482K)$ [36], although in practice evaporation was reported to begin at around $160°C$ $(433K)$ in exploratory evaporations for DEAP at Queen's University in Canada [23]. The molecule has a diameter of around $d = 1220pm$. The equation for mean free path will be

$$\lambda = \frac{k_B T}{\sqrt{2}\pi d^2 P}$$

where T is the temperature, P is the pressure, and k_B is the Boltzmann constant. By plotting the mean free path against the pressure we can determine what pressures are required for different cruicible-to-slide separations. For mean free path of 0.16m (the maximum vertical height available for evaporation inside the bell jar), at a temperature of $480K$ TPB requires a pressure of $4.7 \times 10^{-5} Torr$, as shown in the plot below.

There were initial problems with leaks, impurities and faulty ion gauges, but these were resolved using leak detectors, multiple cleanings and o-ring and ion gauge replacements. With the aid of liquid nitrogen to help cool the diffusion pump, the evaporator was able to reach pressures in the range of $1 \times 10^{-6} Torr$, which is more than is required for the TPB. Most evaporations were performed at higher pressures - usually around $7 \times 10^{-6} Torr$ - due to the 7 or 8 hours plus required to reach the lowest achievable pressures and those extremes being more than was required.

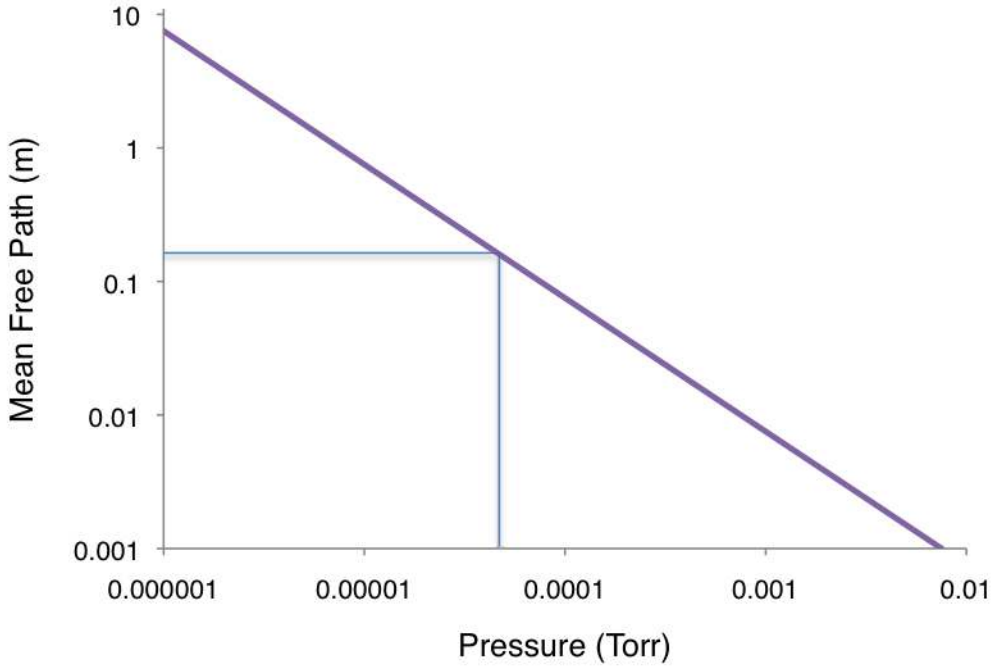

Figure 12: The mean free path of TPB plotted for a temperature of $480K$ and a molecular diameter of 1220pm. The blue line marks the required pressure of $4.7 \times 10^{-5} Torr$ for a mean free path of 0.16m.

2.3 Apparatus

The TPB was placed inside a small cylindrical ceramic crucible $2.8 \pm 0.2cm$ deep with an interior diameter of $0.7 \pm 0.2cm$. The crucible was then surrounded by an electrical heating wire, which in turn was connected to a DC voltage supply. A voltage was then applied across the wire, which generates ohmic heat. The current was increased until the temperature inside the crucible reached the TPB's evaporation temperature. Installing a temperature sensor close enough to the crucible to produce a representative reading of the temperature inside proved difficult, so instead the voltage was simply increased until TPB could visibly be seen appearing on the acrylic slide, which was held $10.0 \pm 0.5cm$ above the crucible in an optical mount.

The acrylic slides used to evaporate on to were cut by the University of Sussex workshop to be $5.1 \pm 0.1cm$ in diameter, with 5 removable $1.1 \pm 0.1cm$ smaller discs cut out of them. These smaller discs were made to fit on the mounts for the department's atomic force microscope (AFM). TPB can therefore be evaporated on to the complete discs, and then the smaller discs can be removed and mounted on microscope slides. The topography can then be scanned in the AFM to evaluate the smoothness and thickness of the TPB layer at different locations on the slide. Before evaporation small strips of cling film were placed in a X shape across the slide so that, once removed, there is a step from TPB to no TPB on the smaller slides, and the thickness of the TPB can be found using the AFM from the size of that step.

Figure 13: Ceramic crucible surrounded by electrical heating wire.

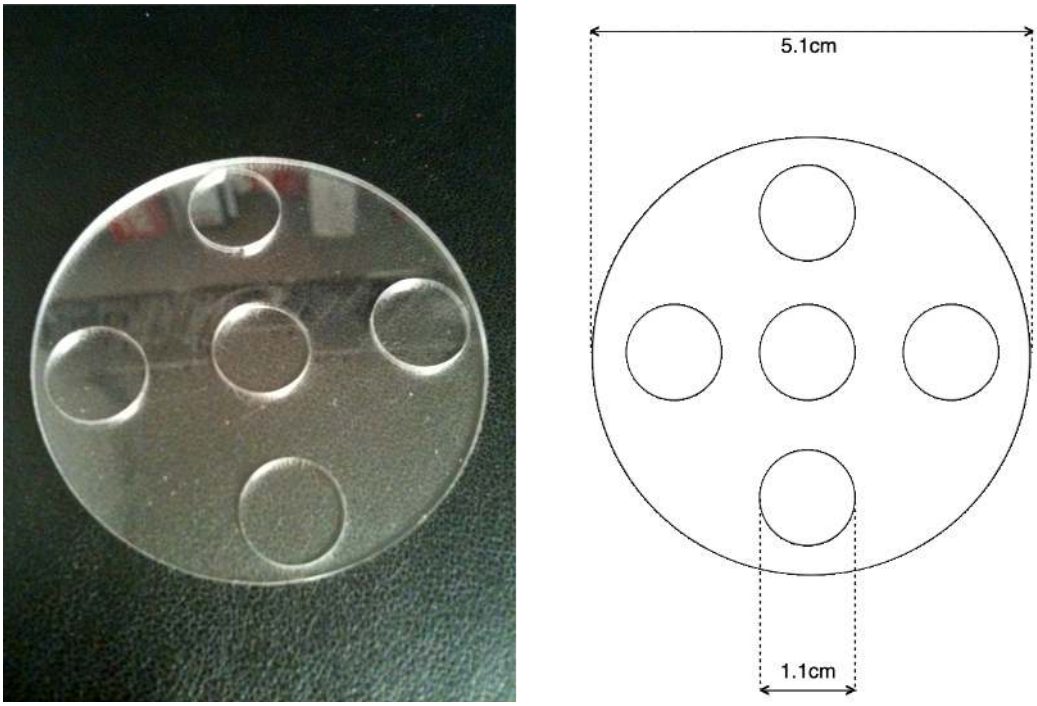

Figure 14: Acrylic discs with five smaller removable discs.

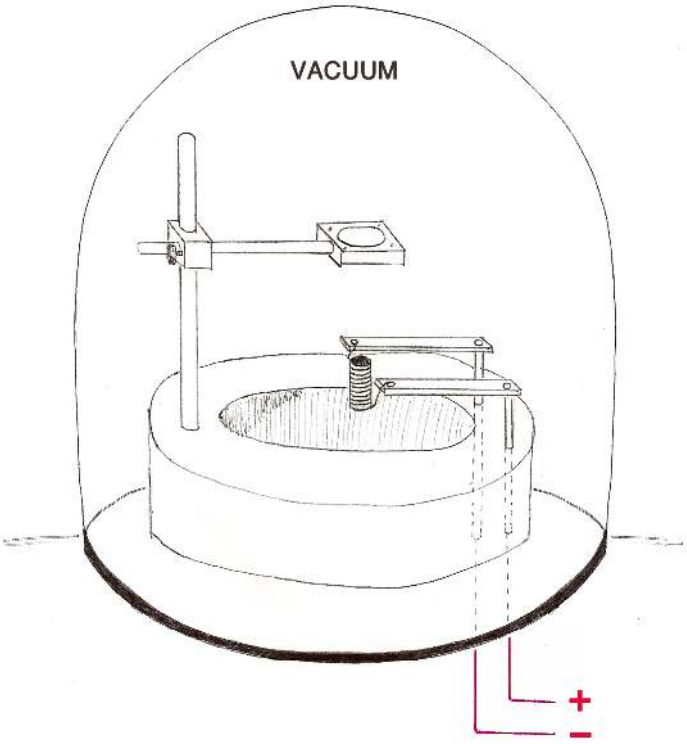

Figure 15: The acrylic slide held above the crucible inside the evaporator's vacuum bell jar. The heating wire around the crucible was then connected to an external DC power supply.

Figure 16: Left: Equipment set up inside the evaporator before the vacuum dome has been added. Right: An acrylic slide after TPB has been evaporated, with the cling film removed leaving strips of TPB-free acrylic. This step can then be used to measure the thickness of the TPB deposit.

Figure 17: Smaller acrylic discs removed and mounted on atomic force microscope slide mounts using pink nail varnish.

The AFM works by gradually raising the mounted sample (via a PZT) beneath a micron thick cantilever. As the atoms on the very tip of the cantilever come close to the atoms on the surface of the sample, the repulsive force causes the cantilever to deflect. An infra-red laser is reflected off the top of the cantilever and into a detector which monitors the beam's location. When a scan is taking place, the cantilever is moved across the sample and changes in topography cause the cantilever to deflect. The AFM recognises the deflection via the laser and adjusts the PZT voltage to alter the height of the sample beneath the cantilever and maintain a constant force between the cantilever and the surface of the sample. These PZT voltage changes are then stored in a pixel grid and calibrated to render a 3-dimensional topographic image of the surface.

The AFM can be used to scan a $7\mu m^2$ window on the surface. Capturing the edge on the transition from TPB to no TPB to measure the step height involved very careful repositioning of the slide beneath the microscope. This took considerable time, but became easier with practice. Best results were achieved by landing the cantilever on the acrylic. Landing on the TPB itself proved problematic, as the AFM's automatic approach function was often confused by TPB debris on the surface. These small TPB fragments were the result of the irreducibly dynamic process of removing the shielding cling film after evaporation. Even after landing the microscope successfully, the TPB debris continued to cause issues in scans, sometimes catching on the end of the cantilever and distorting the resultant image. These appear in the scans as warped ridges and oddly smooth distortions. For the most part scans that featured these were retaken on regions where the cling film had made a cleaner break with the slide on removal.

Quirks of operation aside, the AFM provided an excellent tool for visualising the surface topography of the TPB deposit, but the machine itself is 40 years old, and as a consequence, the calibration, alignment and highly sensitive PZT have become slightly distorted over time. This means the accuracy of vertical measurements are not as good as originally intended. To quantify the uncertainty and to calibrate the AFM as accurately as possible, scans were taken of a calibration grating with a step height of $560 \pm 2.6nm$. The measurements were taken in 10 different locations across 10 different scans of the same grating. The average was then used to calibrate the z-axis. These readings were then repeated to calculate the uncertainty on any height measurement using this apparatus. It was found to be $\pm 21nm$ with a level of confidence of approximately 95%.

2.4 Evaporations: Phase 1

The first evaporation was used to get a sense of what power input to the crucible heating wire was required. The pressure inside the evaporator when heating began was $(2.9 \pm 0.1) \times 10^{-6} Torr$ with a separation between top surface of the TPB crucible and acrylic slide of approximately $5.0 \pm 0.5 cm$. The uncertainty on the height comes from the difficulty in precisely aligning measuring equipment inside the evaporation space. The uncertainty on the pressure comes from the precision of the ion gauge monitor.

Based on the approximate size of the crucible and treating the system as a black body, the power input required to reach a temperature of 170°C ($443.2K$), which is the guideline temperature at which TPB had been observed to begin evaporating in earlier DEAP evaporations [23], was estimated to be 3W. On this run the TPB was observed visually to evaporate within about 5 minutes with a power input of $2.8 \pm 0.1 W$ (Voltage: $5.0 \pm 0.2 V$, Current: $0.55 \pm 0.01 A$ - the uncertainties come from the precision available on the voltage supply and the ammeter monitoring the current).

Below you can see the 3D images of the surface topography of this TPB evaporation, which was captured using the AFM. Based on one scan, there is a variation in topographic height of approximately $1.3 \mu m$. The topographic roughness histogram for each 3D data point was plotted using WSxM 3.1 by Nanotec Electronica S.L, a scanning probe microscopy analysis software. The step profile plot was captured perpendicular to the edge, again in WSxM. A plane removal was used to extract any tilt from the microscope mount, using the flat acrylic surface as a baseline. Based on one scan of this edge, the sample had a thickness of approximately $6 \mu m$. This is clearly far too thick and the gradient makes it tricky to estimate the actual thickness, as it appears to be varying considerably within the $75 \mu m^2$ window. Under the microscope the TPB formed a solid layer, but was covered in small flecks of denser TPB areas, likely due to the rapid evaporation process.

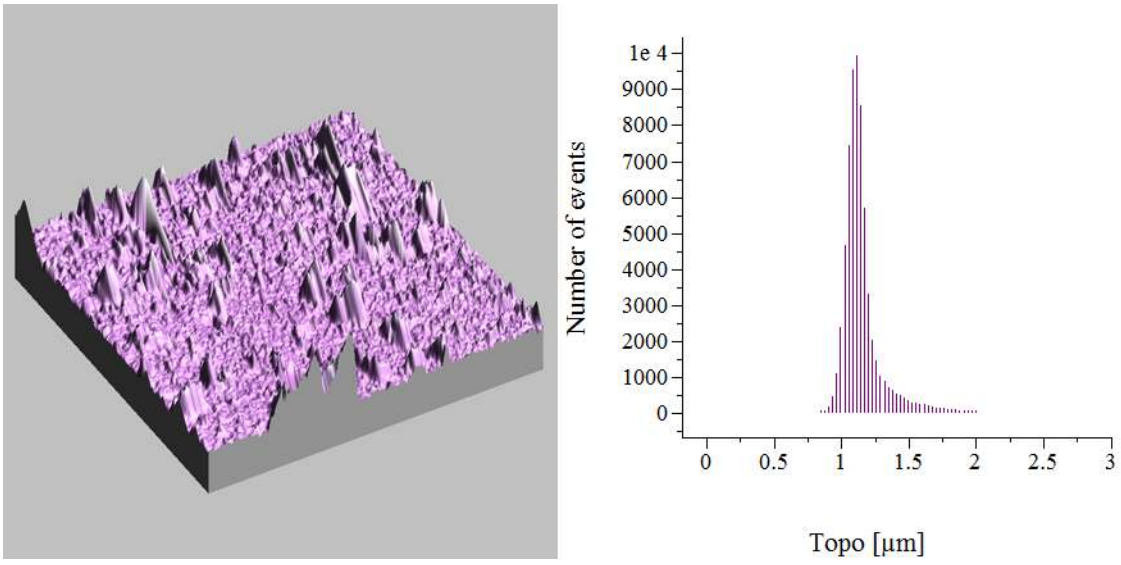

Figure 18: Evaporation 1. TPB coated surface scan captured using atomic force microscopy; histogram of the topographic roughness. This shows a variation of approximately $1.3 \mu m$.

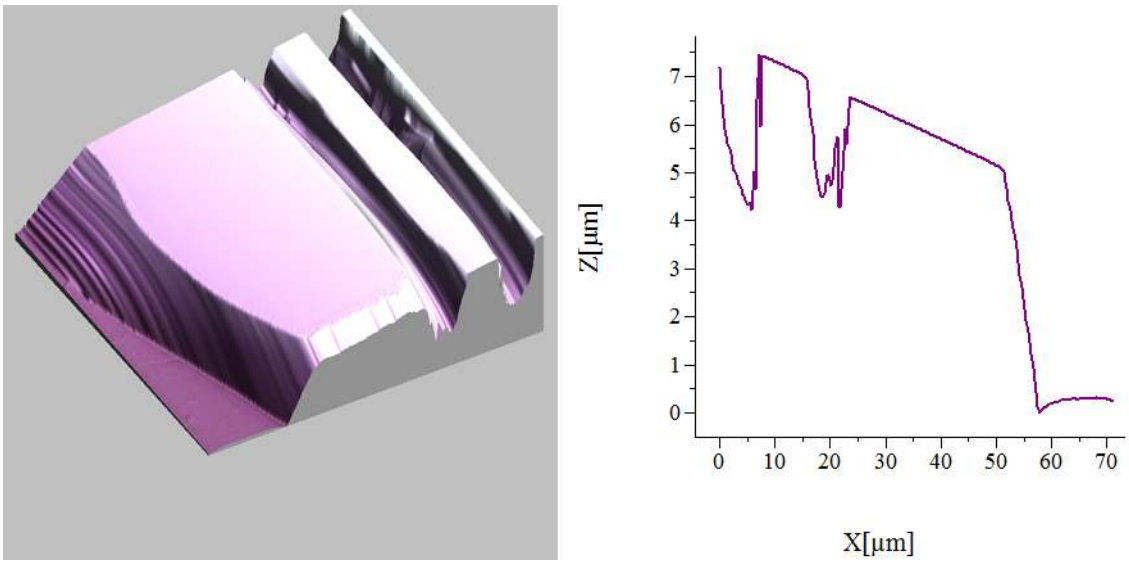

Figure 19: Evaporation 1. TPB coated surface scan capturing the edge of the TPB deposit; profile plot of the topographic height. This shows a TPB thickness of approximately $6\mu m$.

For the next trail evaporation the pressure inside the evaporator when heating began was $(1.5 \pm 0.1) \times 10^{-6} Torr$. The heating wires began with a setting of $0.42 \pm 0.01 A$ and $3.5 \pm 0.2 V$ $(1.5 \pm 0.1 W)$. The hope was that by setting it initially lower than the previously observed evaporation with a power of just $2.8 \pm 0.1 W$, the evaporation point would be approached much more slowly. However, after just 5 minutes on this setting slight fluctuations were observed on the pressure gauge, indicating that something was evaporating. The crucible heating power was left at these settings for 15 minutes, during which there were many little jumps on the pressure gauge - possibly small quantities of TPB explosively evaporating - and the pressure overall increased to $(1.8 \pm 0.1) \times 10^{-6} Torr$.

After these 15 minutes a visible whitening of the slide was observed as TPB solidified on the surface. The evaporation was stopped after a further 10 minutes by pulling a shutter over between the TPB crucible and the slide. Overall, from beginning heating the crucible through to closing the shutter, the evaporation took 25 minutes.

Previous DEAP TPB evaporations at SNOLAB produced a smooth coating by taking around 45 minutes to reach the early stages of evaporation, and then sustaining the temperature a further hour while the TPB evaporated [**?**]. These experiments evaporated a much larger quantity of TPB than for this project, but the 45 minute slow lead up to the evaporation point should be a good guide for the speeds required for a smooth coating.

The 3D images of the surface topography can be found below, showing the deposits were approximately $2.5\mu m$ thick. The histogram of topographic roughness across a TPB coated region shows the deposit has an approximate variation in topographic height of $650nm$, which is a significant improvement on the first evaporation. Through the microscope the sample lacked the obvious TPB dust on the surface of the first evaporation, but still appeared flake-like and crumbly.

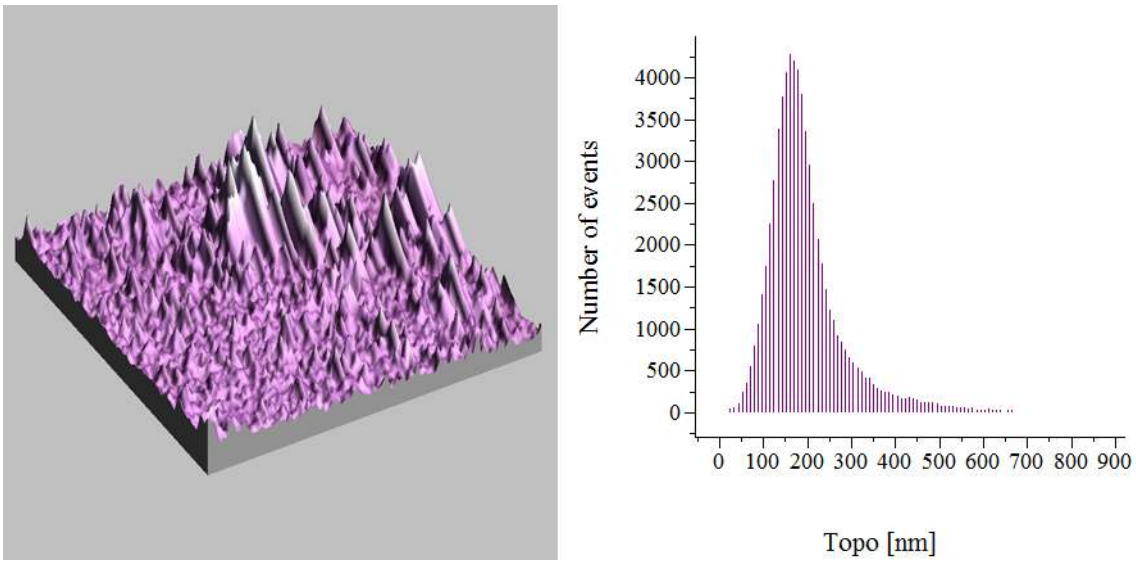

Figure 20: Evaporation 2. TPB coated surface scan captured using atomic force microscopy; histogram of the topographic roughness. This shows a variation of approximately $600nm$.

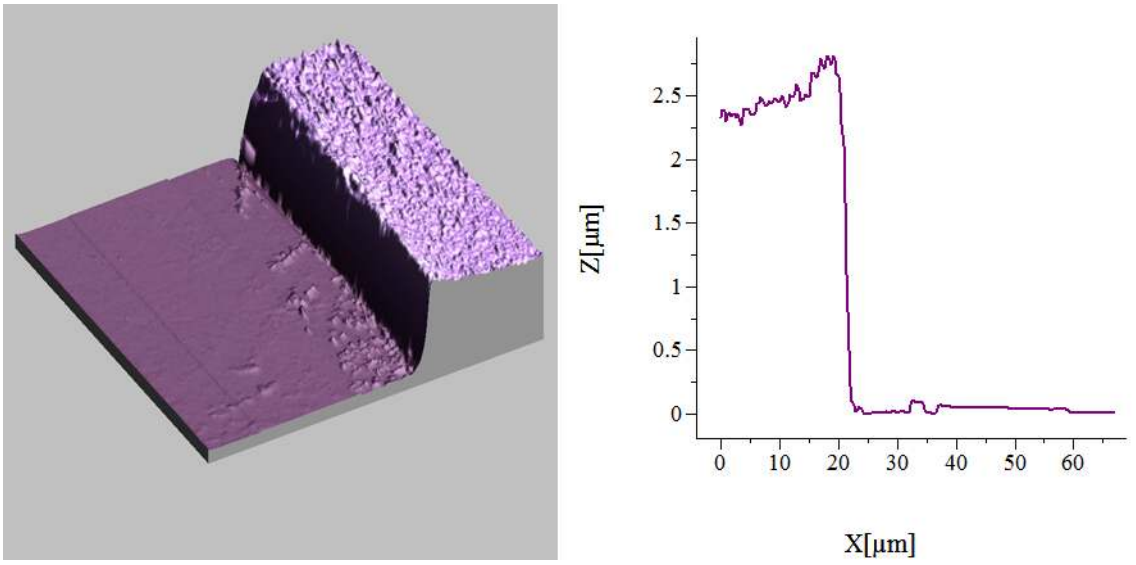

Figure 21: Evaporation 2. TPB coated surface scan capturing the edge of the TPB deposit; profile plot of the topographic height. This shows a TPB thickness of approximately $2.5\mu m$.

Neither of these first two trial evaporations were thin or smooth enough, but the cling film method used to obtain an edge to measure the thickness was successful. At this stage several aspects were identified for improving the quality of the evaporation and allowing greater control over the thickness:

- Several different ways of measuring the temperature inside the crucible were attempted, but it was not sufficiently accurate, and was complicated by the fact that the TPBs evaporation temperature seemed to be much lower than literature values once inside the vacuum. A deposition monitor installed inside the evaporator

would pinpoint and calibrate the input power to deposition rate with much more precision than relying on visual confirmation of TPB appearing on the slide. The moment evaporation begins could be observed exactly and the heating power could be maintained over a longer period to produce a smooth, steady evaporation. It was also possible that this monitor could be used to calculate the exact evaporation time required to produce a desired thickness.

- The flecked bits of TPB dust were thought to be due to mini TPB "explosions" within the main body of TPB in the crucible. At slower evaporating speeds this should not happen, but it was also considered possible that increasing the gap between the crucible and the slide might reduce the impact of these events should they occur.
- During evaporations 1 and 2 we observed a flickering of the pressure on the ion gauge, where the pressure would rapidly decrease for a moment. It is thought these blips corresponded to explosive evaporation activity due to the evaporation being far too rapid. Hopefully with a slower, more controlled heating these rapid pressure fluctuations should be reduced, and their absence from the pressure profile throughout the evaporation should be another indicator of a slower deposition process.

2.5 Deposition monitor

Purpose built deposition monitors are costly and would quickly become clogged with deposit given the number of trial evaporations anticipated to perfect this process. To produce a quick, cost-effective and disposable way to track the evaporation process, a simple deposition monitor was constructed using a mini quartz crystal module. Quartz is a piezoelectric and can be made to distort in the presence of an electric field. This is utilised in these frequency modules by applying a low voltage to an electrode near the crystal and placing it in an electric field, which causes it to distort. When the field is removed, the crystal then generates its own electric field as it returns to its former shape. This allows the crystal to behave like an RLC circuit, generating an oscillating voltage with a very specific resonant frequency determined by the rate at which it distorts and returns to its normal shape.

If mass is added to the surface of the crystal, the resonance frequency is gradually reduced, and the amount of mass added is proportional to the frequency change

$$m_s = m_q \frac{\Delta f}{f_q}$$

where m_s is the mass deposited on the surface, m_q is the mass of the quartz, f_q is the quartz's natural resonant frequency, and Δf is the frequency shift due to the coating on the surface of the crystal. Assuming the new deposit is uniformly distributed on the surface, we can rewrite the mass of the deposit as

$$m_s = d_s \rho_s A$$

where d_s is the thickness of the deposit on the surface, ρ_s is the density of the deposit, and A is the area of the quartz surface. The quartz mass can be expressed similarly

$$m_q = d_q \rho_q A$$

in terms of the density and thickness of the quartz crystal. Substituting all these in and rearranging for the thickness of the deposit on the surface we have

$$d_s = \frac{d_q \rho_q}{f_q} \frac{\Delta f}{\rho_s} = K \frac{\Delta f}{\rho_s}$$

demonstrating that the thickness of the deposited layer is proportional to the change in frequency of the quartz crystal. Here K is a constant that depends entirely in qualities of the original quartz crystal, and ρ_s, similarly, will remain unchanged, as it is a constant of the deposit.

A batch of Vishay Dale Half Size Clock Oscillators were purchased, which have a natural resonant frequency of 4MHz. The workshop then carefully removed the metallic casing to expose the crystal surface. A small rig was constructed to support the module inside the evaporator, and to connect it via emulsion-coated wires to the evaporator's wire output module. Compatible sockets were then purchased and adapted with a bit of soldering to send the signal to an NI USB block, which joined the device to a computer to power the module and monitor the frequency output via a LabView program.

With the module placed right next to the acrylic slide, it was possible to monitor the frequency output as the crucible was slowly heated. The moment the frequency began

to change it would tell you evaporation had begun, and you could stop increasing the power to the electrical heating wires.

One of the advantages of crystal oscillators is that the frequency signal is very clean and noise free. However, once the signal had been passed through the soldered wiring connections required to adapt the deposition module rig to the 30-year-old adaptors of the evaporator, the signal was significantly distorted, and the LabView software was no longer able to read the frequency. This distortion was identified by wiring everything up to an oscilloscope to observe the shape of the signal output, and see how it changed as different connecting components were introduced to the circuit.

This problem was fixed by placing a variable resistor between the signal and ground of the module output. This allowed an impedance match to the additional load added by the connecting wires. It was found that a 100Ω resistance cleaned the signal up nicely, so a small resistor was introduced to the module rig on the connections to the NI USB block joining the device to the LabView computer.

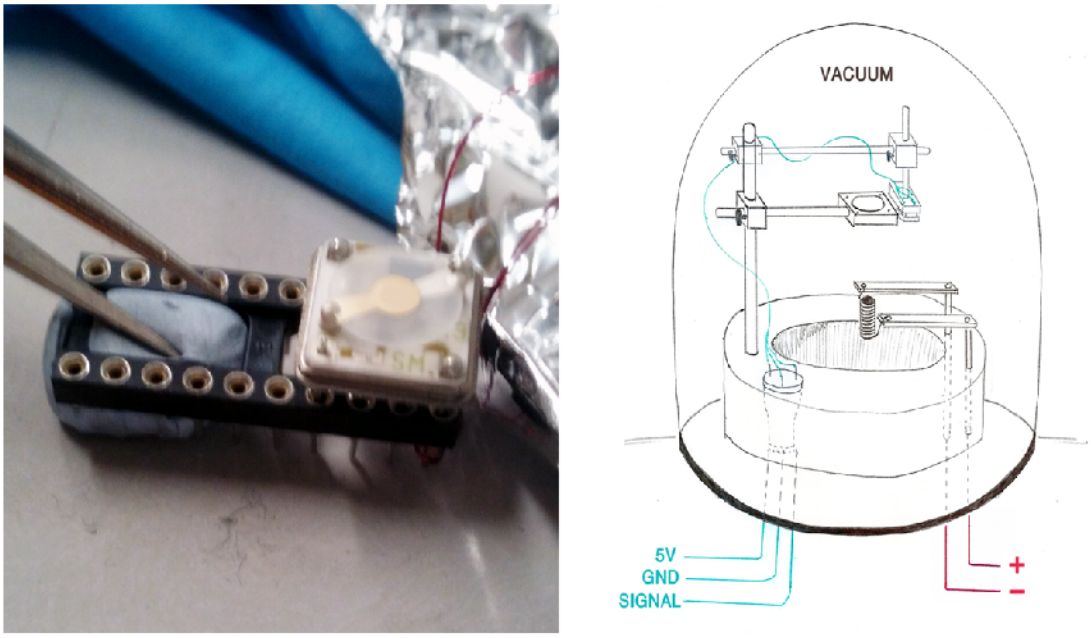

Figure 22: Left: the deposition module with the exposed quartz crystal, plugged into a small mount, which is soldered to emulsion-coated wires. Right: Modified equipment layout with the deposition module installed alongside the acrylic slide mount.

Before attempting to evaporate with the deposition module in place, a few dry runs were performed to see how it would respond to being placed in the vacuum and beneath the heated crucible. Across the course of this run, the crucible was heated up to TPB evaporation range with no TPB inside. The frequency readout can be seen below. It was, for the most part, very stable on the order of a few Hz, with very slight fluctuation. There are three jumps lasting no more than a few seconds. These correspond to isolated disruptions within the vacuum. The first was when the ion gauge was turned on, the second when it was turned off, and the third when the vacuum was released.

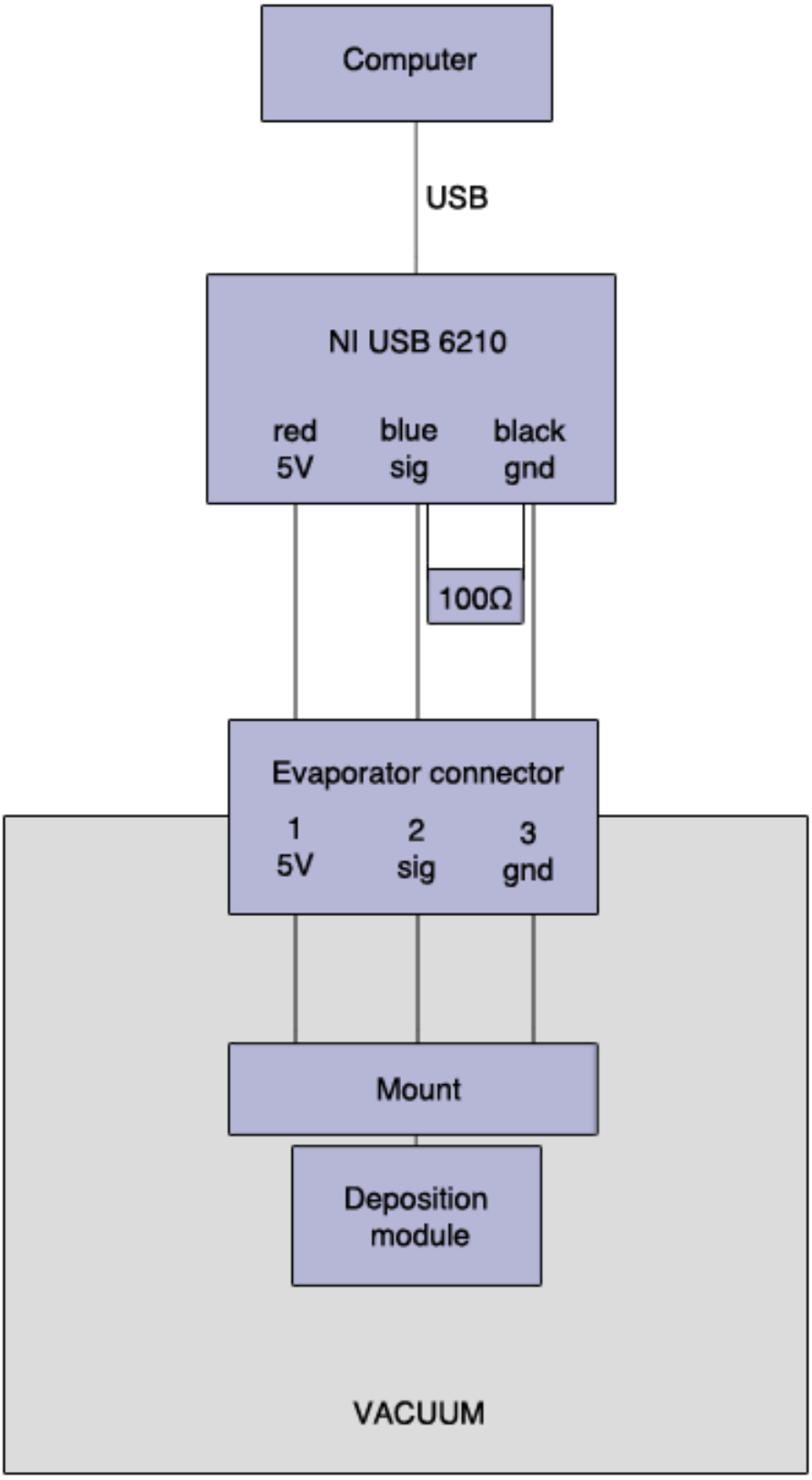

Figure 23: Block diagram of the circuit setup for powering the deposition module inside the evaporator via LabView.

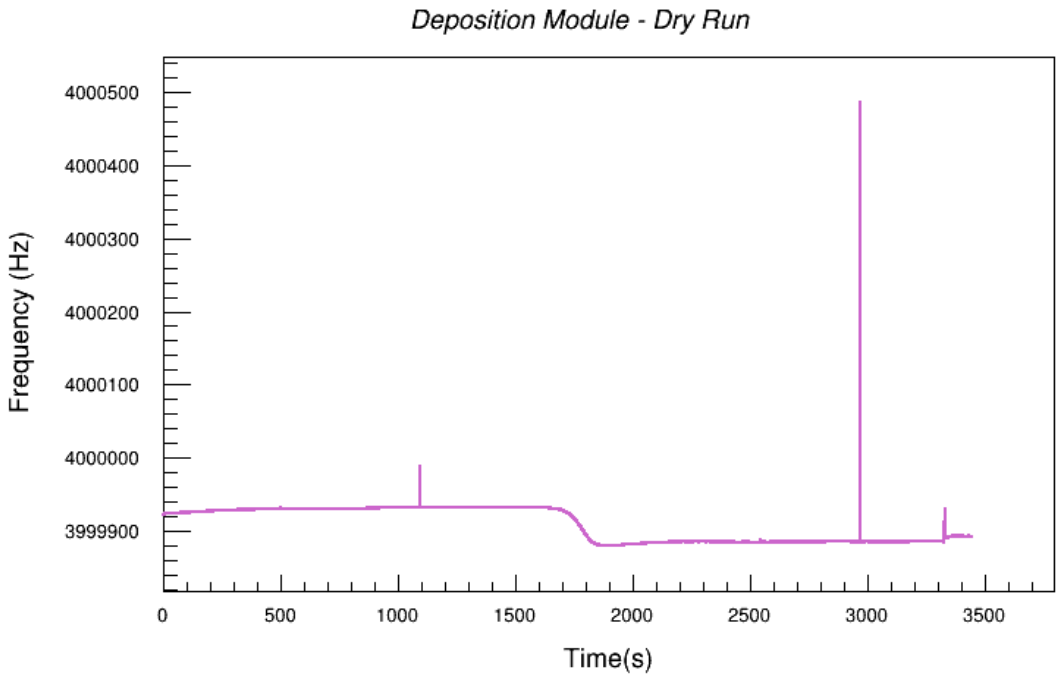

Figure 24: The large blips in correspond, in chronological order, to (1) turning the ion gauge on; (2) turning the ion gauge off; (3) opening the vacuum. The slow dip that permanently alters the otherwise fairly stable frequency at around $1800s$ is thought to be due to residual TPB in the crucible being evaporated and deposited on the quartz crystal, thus generating the kind of frequency shift we would expect.

The other major feature of this plot is the slow and permanent frequency change that occurs at around the $1800s$ mark. No TPB was in the crucible, as this was a dry run, but it was postulated that this frequency shift corresponded to residual TPB evaporating up on to the crystal. This change occurred with $3.0 \pm 0.2V$ and $0.38 \pm 0.01A$ supplied to the heating wire, and was used as a guide for when to expect evaporation to begin when the next phase of evaporations were attempted.

It should be noted that it is not known precisely how many depositions can be completed before the build up of TPB on the quartz crystal causes the linear relationship between frequency and mass deposited to break down. However, the frequency output was closely monitored for any non-linear behaviour throughout all evaporations. Only three quartz modules were used for the duration of this project, and the first two both stopped behaving linearly once the frequency dropped below 3.9MHz. This point was identified on the frequency read out as an inability to reach a stable equilibrium temperature. There is always some slightly variation for the first 30 minutes after the module is turned on, and while the vacuum is forming, but it should then proceed to behave very linearly. As soon as it ceases to stabilise, the module needs replacing.

2.6 Evaporations: Phase 2

This evaporation was performed at a starting pressure of $(8.8 \pm 0.1) \times 10^{-6} Torr$ and a starting deposition module frequency of $3999882 Hz$. This was slightly lower than the quartz's resonant frequency of $4 MHz$, as the module had previously been used in the dry run, so some residual TPB from that trial remained on the surface.

The slide, with deposition module next to it, was mounted 7 ± 1cm above the top of the crucible, increasing the separation slightly to reduce the impact of explosive evaporations, should they occur. The voltage and current were then slowly increased, approaching the settings where deposition had been observed in the trial run. The frequency of the module output began to decrease with $2.5 \pm 0.2 V$ and $0.32 \pm 0.01 A$ through the electric heating wires, indicating that evaporation had begun. The settings were then left at exactly that level for 160 minutes so the TPB could slowly evaporate up onto the slide.

Across this time there were no observed sudden fluctuations in the pressure, as seen with previous evaporations. This indicated a reduction in explosive evaporation activity due to slower heating.

After 160 minutes the slide appeared visually misted with the TPB deposit. Across this time the frequency had decreased to $3996564 Hz$, corresponding to a Δf of $3318 Hz$. The evaporation was stopped at this point by turning a mechanical shield to block the path between the crucible and the slide. The vacuum was then slowly released after waiting 30 minutes or so to allow the crucible to cool. The frequency readout from the module across the entire run is shown below. It is clear that it behaves very linearly.

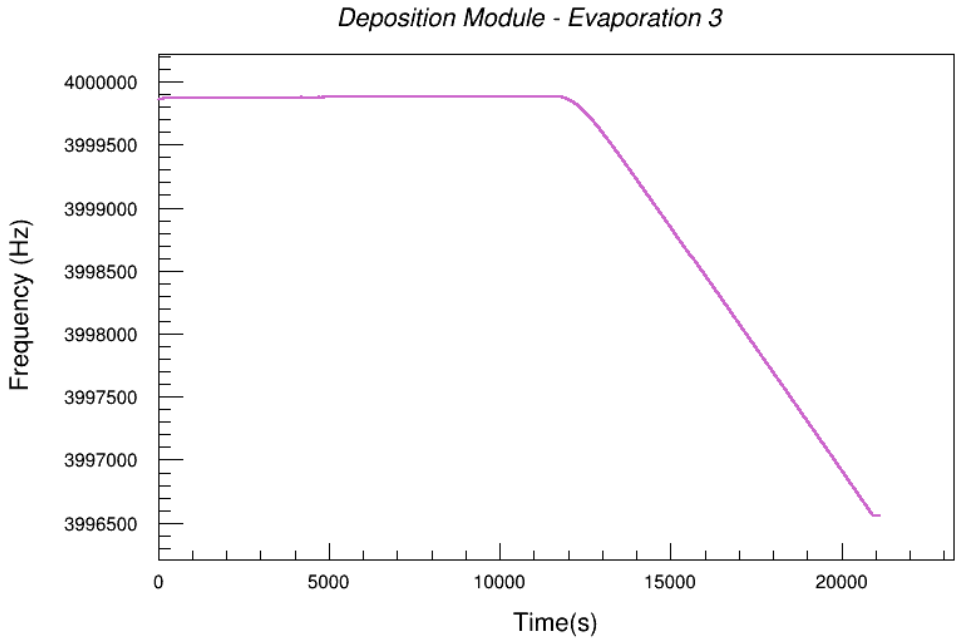

Figure 25: The frequency module readout for the evaporation 3 showing a very linear frequency decrease of 3318Hz across the entire evaporation.

An AFM scan of the surface of the TPB deposit from this evaporation can be seen below. It shows a variation in vertical height of approximately $400nm$, and a thickness of $0.57^{+0.09}_{-0.05}$ μm. This was found using the *measure distance* feature on the WSxM software which measures the height difference between two locations on the AFM scan. The height difference was measured from $10\mu m$ either side of the step at ten different locations along the TPB step. A screenshot below shows how this process is implemented in the software. These ten different values for the step height were then averaged to give an estimate of the TPB layer thickness.

The uncertainty of $21nm$ per AFM height measurement (calculated using the grating), is significantly less than the variation observed across these ten readings of the step size in one individual scan, which displayed a range of $0.147\mu m$ around the average. Therefore, when quoting the average thickness of a height step I will include the maximum positive and minimum negative variation observed either side of the average from the ten readings. Areas of the step that were visually observed through the microscope to be badly damaged by the cling film removal were avoided where possible. It is hoped that by always measuring $10\mu m$ behind the step edge, the impact of the major vertical distortions at the edge of the step is minimised.

Ultimately, this limitation on the accuracy of the thickness measurements is not a huge problem. The requirement is that the deposition be measured to be on average $0.9\mu m$ not varying by more than 30% across the slide. It should be perfectly feasible to confirm this has been achieved with the available accuracy of this method.

This deposition was actually thinner than the desired thickness, indicating that it is definitely possible to slow the TPB evaporation process sufficiently. The topographic roughness is still slightly more than desired, but the TPB surface visually appears much improved under the microscope in terms of smoothness of distribution. The slower evaporation clearly improves the quality of the deposit and the thickness can now be much more carefully controlled.

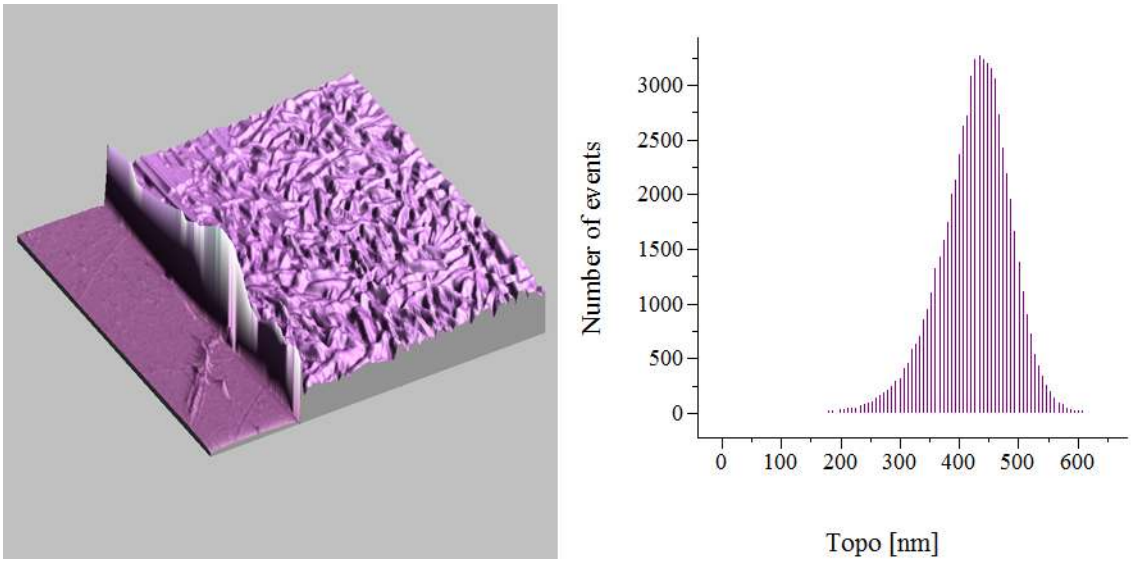

Figure 26: Evaporation 3. TPB coated surface scan capturing the edge of the TPB deposit; histogram of the topographic roughness showing a variation of approximately $400nm$.

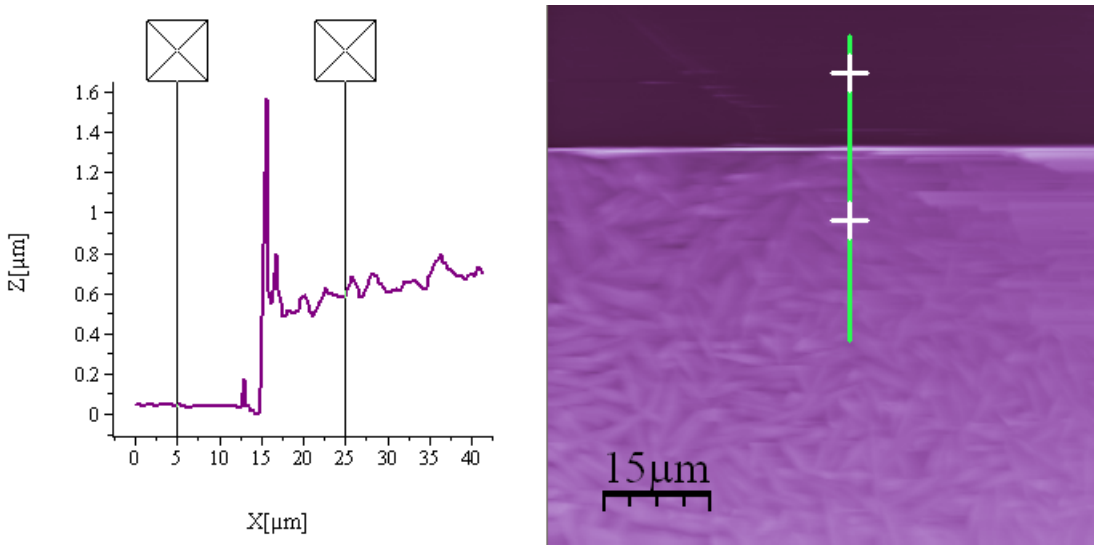

Figure 27: Evaporation 3. Screen shot of the step height measuring process in the WSxM software with points marked on a 2D view of the top of the scan and on the profile where the height difference will be measured. These points are located $10\mu m$ either side of the step. Each measurement was repeated 10 times at different locations across the scan.

The results of this evaporation were then used to calibrate the frequency change to deposit thickness using the relationship explored earlier.

$$d_s = K\frac{\Delta f}{\rho_s} \quad \longrightarrow \quad \frac{K}{\rho_s} = \frac{d_s}{\Delta f}$$

$$\sigma_{\frac{K}{\rho_s}} = \sqrt{\left(\frac{1}{\Delta f}\right)^2 \sigma_{d_s}^2 + \left(\frac{d_s}{\Delta f^2}\right)^2 \sigma_{\Delta f}^2}$$

From this evaporation:

$d_s = 0.57^{+0.09}_{-0.05} \times 10^{-6} m$
$\Delta f = 3318 \pm 5 Hz$

The uncertainty on Δf comes from the rate of change of frequency and the time taken to recognise that evaporation had started, and to put the shield across and end it. This uncertainty is actually insignificant compared to the massive uncertainty in the height measurement from the AFM, but was included for completeness.

$$\frac{K}{\rho_s} = 1.7^{+0.3}_{-0.2} \times 10^{-10} m Hz^{-1}$$

This was then used to calculate the deposition module frequency change required for the desired thickness of deposit using the relation:

$$\Delta f[Hz] \ = \frac{1}{1.7 \times 10^{-10}} d_s[m]$$

So for a thickness of $0.9\mu m$ a frequency change of $5240^{+830}_{-500}Hz$ was required. Unfortunately this is quite a large frequency range, due to the uncertainty in the height readings from the AFM. However, this calculation was based on just one scan of the surface of the evaporated TPB. Repeat evaporations and calculations were required to confirm that this method was reliable.

It became necessary at this stage to start looking at the TPB distribution across the surface of the disc by taking scans from multiple different locations using the smaller removable discs near the edges. Given the difference between the opening of the crucible and the size of the acrylic slide, and the separation between the two, the TPB layer was not expected be uniform across the slide, and this needed to be investigated.

Another evaporation was performed with exactly the same setup to try and replicate the performance of the third evaporation, to check that the deposition monitor continued to perform linearly, and to check that it was possible to generate a consistent relationship between frequency change and thickness of deposit. The evaporation began with a pressure of $(3.0\pm0.1)\times10^{-6}Torr$ and a frequency output of $3996522Hz$. The evaporation was stopped at a frequency of $3992463Hz$ corresponding to a frequency change of Δf of $4048Hz$. The evaporation again took about 160 minutes.

Topographic scans of the surface of this slide were taken in five separate places corresponding to the locations of the five different removable discs, so one in the centre and four at the edges. Scans were taken as near to the middle of each removable disk as possible. As with the previous evaporation, ten repeat readings were taken of the height difference across the step, and these were then averaged. The deposit thicknesses and vertical variation are summarised in the table below and in a simple bar chart. It should be noted that all of the "edge" measurements were taken from positions exactly the same distance radially outwards from the centre, just on four different sides of the slide.

slide	TPB thickness	height variation
centre	$0.77^{+0.07}_{-0.06}\mu m$	500nm
edge 1	$0.55^{+0.03}_{-0.03}\mu m$	400nm
edge 2	$0.54^{+0.04}_{-0.03}\mu m$	300nm
edge 3	$0.45^{+0.02}_{-0.02}\mu m$	400nm
edge 4	$0.27^{+0.03}_{-0.02}\mu m$	400nm

Again the overall the deposition was not quite thick enough. It is also clear there is a definite distribution across the slide, with a thicker layer in the middle, decreasing to the outside. It was not clear why one of the samples, edge 4, was so much thinner than elsewhere. It is possible the area where the edge captured in the AFM was damaged by the cling film removal process in a way not obviously visible through the microscope, or that it was somehow partially shielded during evaporation by a stray piece of cling film.

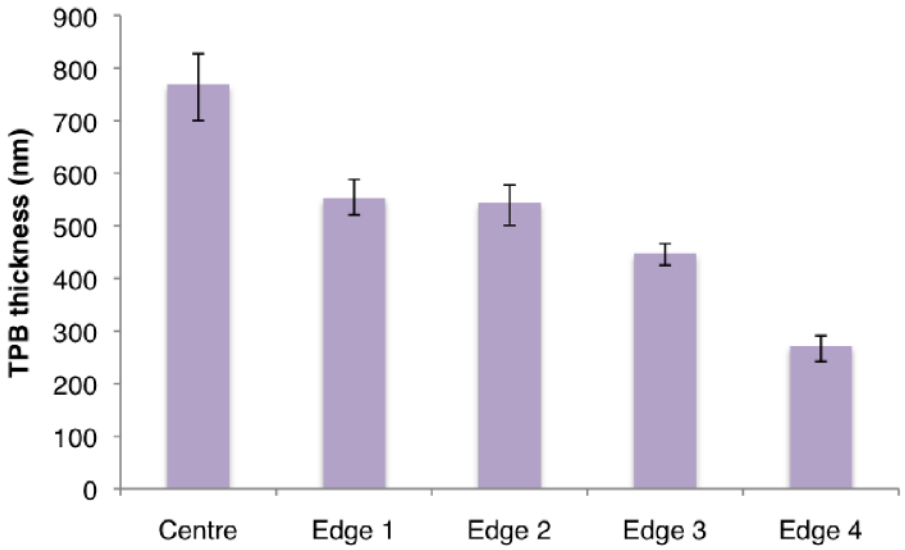

Figure 28: Evaporation 4. Location and TPB depth from the five separate scans at different locations on the surface of the slide.

As before, it was possible to calculate the frequency-to-thickness constant using these results. This calculation was performed using the thickness measurements from the centre of the slide, to check that it was consistent with the previous evaporation.

$d_s = 0.77^{+0.07}_{-0.06} \times 10^{-6} m$
$\Delta f = 4048 \pm 5 Hz$

$$\frac{K}{\rho_s} = \frac{d_s}{\Delta f}$$

$$\frac{K}{\rho_s} = 1.9^{+0.2}_{-0.1} \times 10^{-10} m Hz^{-1}$$

$$\Delta f[Hz] = \frac{1}{1.9 \times 10^{-10}} d_s[m]$$

This suggested a frequency change of $4730^{+430}_{-370} Hz$ was required to produce a layer that is $0.9 \mu m$ thick. The range of frequencies calculated here falls within the range from evaporation 3, which found a frequency change of $5240^{+830}_{-500} Hz$ was required. So, this method of estimating the required frequency for a given deposition thickness was consistent, although not particularly accurate, given the range of AFM heights observed.

2.7 Spacial thickness distribution

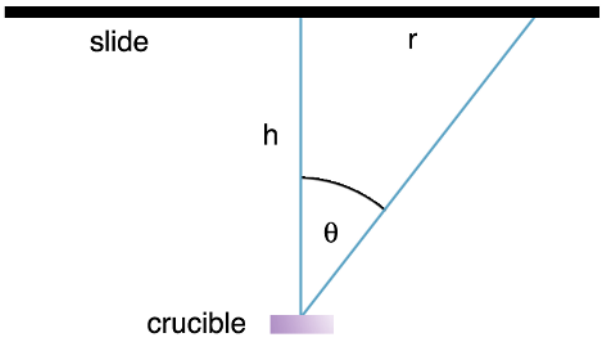

Figure 29: Geometry of the crucible-to-slide set-up

When the TPB molecules are evaporated under a vacuum, the thickness of the TPB layer formed when it is deposited on the slide will depend on the distance from the crucible to the substrate, and the radial distance from the axis of the crucible. In evaporation 4 there was approximately $0.2\mu m$ difference from the thickness of the TPB deposit at the centre of the slide, vs $2cm$ out towards the edge of the slide. To make the slides as uniform as possible the effect of this distribution needed to be reduced.

This distribution was modelled by assuming a small surface area source, i.e. the top surface of the crucible, evaporating on to a flat surface. The model incorporates the distance from the crucible to the slide, h, the radial distance on the slide from the axis of the crucible, r, the density of TPB, ρ, the rate of evaporation in kg/s, v_e and the angle θ between a vertical line along the axis of the crucible and a line to the radial point on the slide. The rate of deposition, v_d, in ms^{-1} can be expressed as

$$v_d = \frac{v_e}{\pi\rho(h^2 + r^2)} cos^2(\theta).$$

If the rate of deposition is assumed constant, it can be expressed as d/t, where d is the thickness of the finished deposition and t is the time the deposition took. Using the results from evaporation 4, i.e. the deposition thickness at different radii, the geometry of the setup, and the time the deposition took, all the constants of this equation can be estimated. You can then express the deposition thickness as a function of the separation between the source and the substrate and the radial distance.

$$d = A\frac{t}{(h^2 + r^2)} cos^2\left(tan^{-1}\left(\frac{r}{h}\right)\right)$$

where

$$A = \frac{v_e}{\pi\rho}.$$

For evaporation 4 we find $A = 4.8 \times 10^{-13}$ for the thickness measurements in the centre of the slide. This can then be used to calculate the difference in thickness between the centre of the slide, at $r = 0$, and centre of one of the smaller removable discs nearer the edge, at $r = 2cm$ for different source to substrate separations, d. The results are plotted below for a range of separations from the $7cm$ of evaporation 4, to the maximum

possible separation in the evaporator of 16*cm*. As the separation increases, the variation in deposition thickness across the surface of the slide decreases. This model suggested it would be very beneficial to increase this distance to the maximum possible to reduce the TPB distribution on the surface.

A 3D plot of the predicted deposition thickness across the area of the slide was also generated using a Monte Carlo script written by Steve Churchwell. This is included below after incorporating the parameters of this experimental setup.

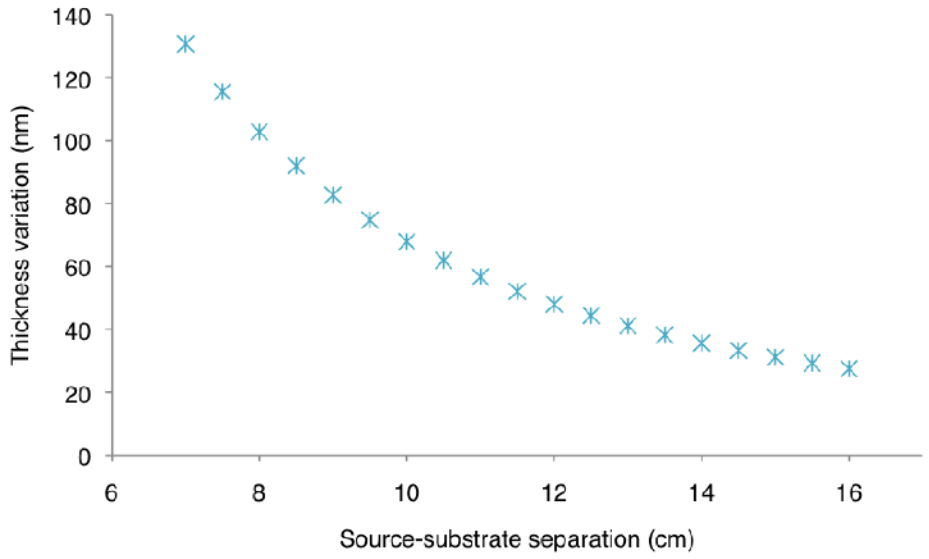

Figure 30: Plot of the changing difference in thickness between the centre and edge of the slide as a function of the source-to-substrante separation. We see that as the slide and the crucible become further apart, the variation in vertical height across the slide decreases.

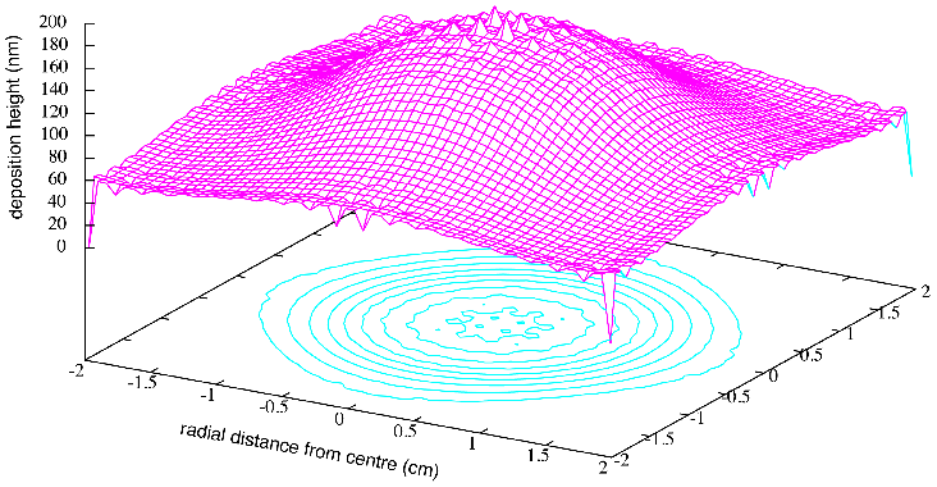

Figure 31: Monte Carlo 3D plot of the deposition thickness variation across the surface of the slide with a 7*cm* separation between source and substrate. This plot was created using data from a Monte Carlo script written by Steve Churchwell

2.8 Evaporations: Phase 3

The aim of these evaporations was to test the apparatus with a larger separation between source and substrate. The distance was set at the maximum possible inside the evaporator vacuum, which is $15.5 \pm 0.5cm$. Because the separation was greater, the rate of deposition on the slide was slower, because the TPB was being dispersed over a larger area as it evaporated out. This also meant that more TPB was effectively wasted in the evaporation, so more TPB was required in the crucible initially to ensure sufficient coverage of the slide. The crucible was filled with TPB each time to approximately $0.5cm$ below the top of the crucible opening. The TPB needed to be encouraged down into the crucible with tweezers to make enough room, but it was not excessively compressed.

To avoid an unnecessarily long evaporation time, the temperature was increased until the gradient of the frequency readout from the quartz deposition module set a reasonable rate. Several trial evaporations were performed to determine the ideal settings. This was tricky as the rate of evaporation changed rapidly with very slight changes in the electrical power input. This is also complicated by the fact that it takes approximately 10-15 minutes for the evaporation rate to respond to the change in crucible heating power, so it is difficult to keep stable. Ultimately it was found that heating wire settings of $4.0 \pm 0.2V$ and $0.42 \pm 0.02A$ produced a frequency change of approximately $3Hzs^{-1}$ on the deposition monitor for the initial hour of the evaporation. This allowed for a reasonable evaporation time of approximately 2 hours with this source to substrate separation. The current was often increased to up to $0.44 \pm 0.02A$ for the final 20 minutes when the remaining TPB in the crucible had lost contact with the edges, so the rate of evaporation slowed.

The first successful trial evaporation was performed with this new setup at a pressure $(6.6 \pm 0.1) \times 10^{-6}Torr$ and saw a frequency shift of $27933Hz$. The thickness of the deposition was then measured at different locations across the slide, as before for evaporation 4. The results are in the table below and show a clear improvement in the spread of thickness distributions across the slide, with an average thickness of $0.79^{+0.05}_{-0.06} \times 10^{-6}m$, so varying by $0.11\mu m$. This would be well within acceptable varying range (30%) if the deposition was on average $0.9\mu m$ thick. Unfortunately it was around $1\mu m$ too thin, so it was necessary to evaporate again and adjust the frequency variation to try and get closer to the ideal thickness.

slide	TPB thickness
centre	$0.83^{+0.02}_{-0.02}\mu m$
edge 1	$0.73^{+0.02}_{-0.02}\mu m$
edge 2	$0.74^{+0.02}_{-0.02}\mu m$
edge 3	$0.76^{+0.02}_{-0.02}\mu m$
edge 4	$0.78^{+0.02}_{-0.03}\mu m$
average	$0.79^{+0.05}_{-0.06}\mu m$

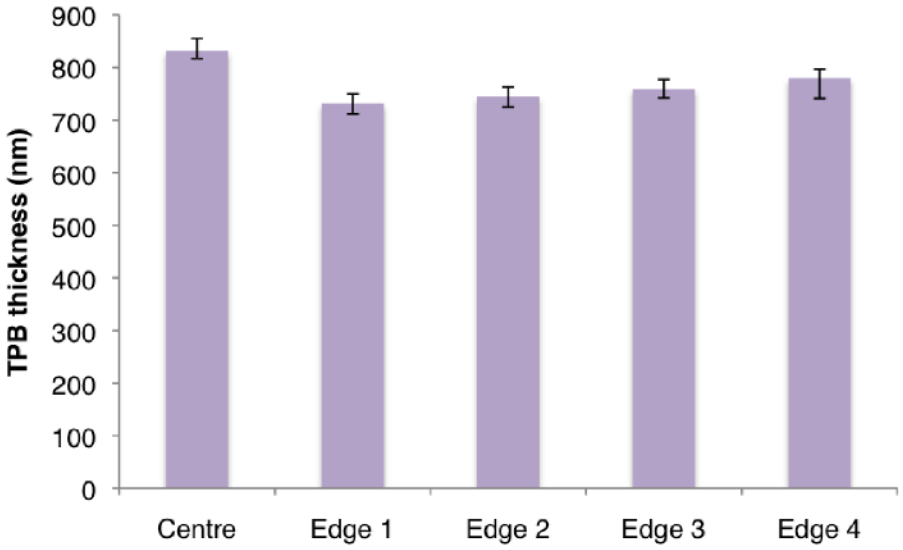

Figure 32: Evaporation 5. Location and TPB depth from the five separate scans at different locations on the surface of the slide.

As before, the required frequency change for the $0.9\mu m$ thickness was calculated from the results of the latest evaporation using the average height observed.

$d_s = 0.79^{+0.05}_{-0.06} \times 10^{-6} m$
$\Delta f = 27933 \pm 5 Hz$

$$\frac{K}{\rho_s} = \frac{d_s}{\Delta f}$$

$$\frac{K}{\rho_s} = 2.8^{+0.2}_{-0.3} \times 10^{-11} m Hz^{-1}$$

$$\Delta f[Hz] = \frac{1}{2.8 \times 10^{-10}} d_s[m]$$

$$\Delta f[Hz] = \frac{1}{2.8 \times 10^{-10}} 0.9 \times 10^{-6} m = 31822^{+2014}_{-2819} Hz$$

A final test evaporation was then performed to try and achieve the required thickness even more precisely. The evaporation was carried out at a pressure of $(6.8 \pm 0.1) \times 10^{-6} Torr$ and saw a frequency shift of $31857 Hz$. The thickness was measured across the slide and found to have an average depth of $0.91^{+0.11}_{-0.07} \times 10^{-6} m$. This result was considered a successful demonstration of the thickness control made possible by the frequency deposition monitor.

With a crucible-to-slide separation of $15.5 \pm 0.5 cm$, a frequency shift of$31822^{+2014}_{-2819} Hz$ produced a deposition that is on average $0.9\mu m$ thick, varying by $+0.1\mu m$ and $-0.07\mu m$. This is well within accepted parameters for the DEAP-3600 detector. It should be noted that much of this variation measured here is thought to be due to disturbances in the cling film removal, so the actual variation across the slide may be much less than quoted.

slide	TPB thickness
centre	$0.95^{+0.02}_{-0.02}\mu m$
edge 1	$0.82^{+0.05}_{-0.02}\mu m$
edge 2	$0.85^{+0.03}_{-0.03}\mu m$
edge 3	$0.89^{+0.03}_{-0.02}\mu m$
edge 4	$0.79^{+0.03}_{-0.02}\mu m$
average	$0.91^{+0.11}_{-0.07}\mu m$

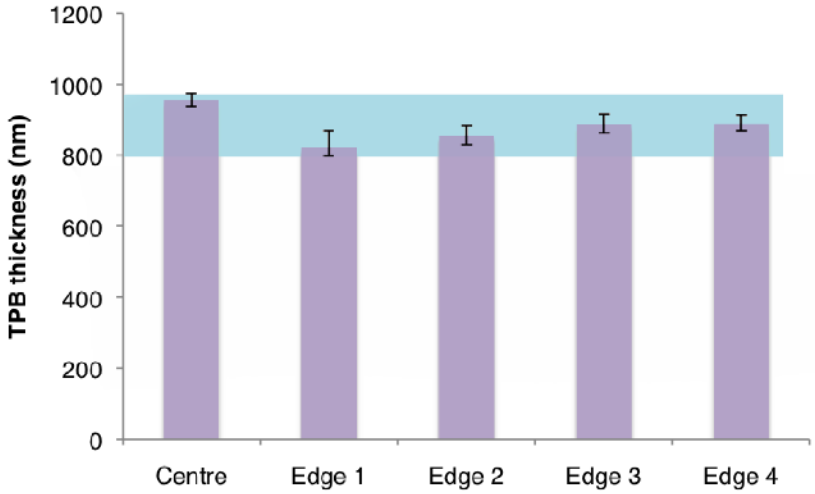

Figure 33: Evaporation 6. Location and TPB depth fon the surface of the slide. The blue band indicates the entire range of measured thicknesses around an average of $0.9\mu m$

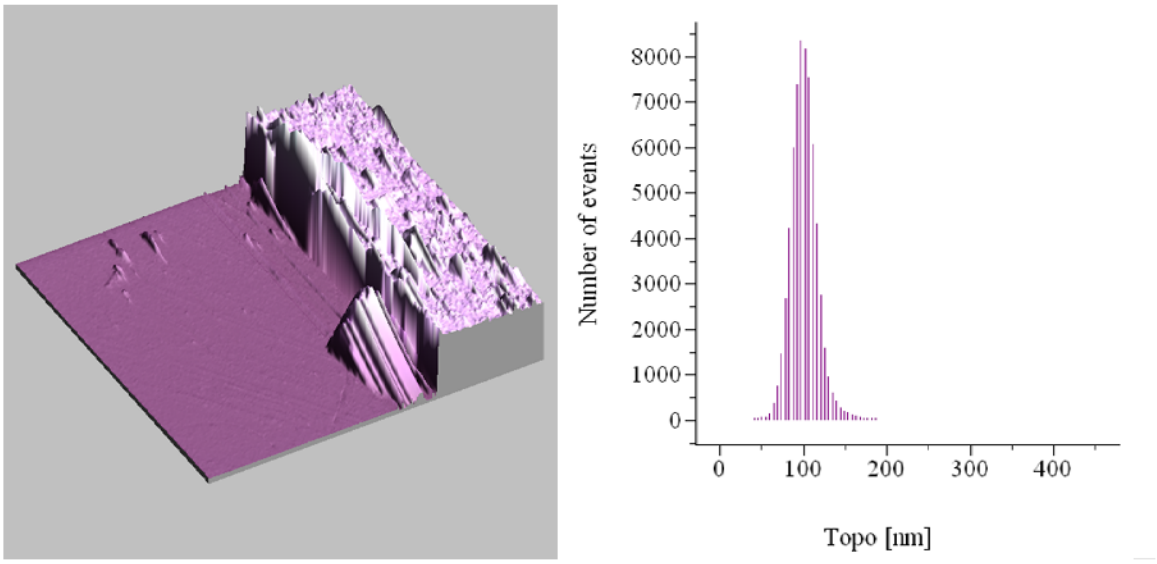

Figure 34: Evaporation 6. TPB step from the centre scan measured to be $0.95^{+0.02}_{-0.02}\mu m$; histogram of the topographic roughness on an area of the TPB surface. This shows a variation of approximately $150nm$, well within the allowed variation range.

2.9 Evaporations: Phase 4: Sanded acrylic slides

The final stage of this experiment was to evaporate on to samples of sanded acrylic identical to those used in the detector. Pre-cut and sanded discs were brought over from the experiment at SNOLab in Canada. Once they arrived at Sussex they were rinsed in ultra pure water, and then left to sit in a bath of ultra pure water for 15 minutes. All contact with alcohol and other solvents was avoided, as they can damage the acrylic. They were then carefully dried with KIM wipes and mounted in the evaporator. The slides were handled throughout whilst wearing disposable nitrile gloves, to prevent the transfer of grease or any fingerprint marking of the acrylic surface.

The evaporation was then repeated exactly as in the trial evaporations, with a crucible to slide separation of $15.5 \pm 0.5cm$, a pressure of $(6.8 \pm 0.1) \times 10^{-6}Torr$ and a total observed frequency shift of $31800 \pm 50Hz$. In total, two separate sanded acrylic slides were evaporated on to for use in calibration testing. An image of one of the evaporated slides can be seen below.

Figure 35: One of the sanded acrylic slides with TPB evaporated on to the surface.

2.10 Conclusions

Listed below are the results of all of the 6 major test evaporations performed, along with pressure, crucible to slide separation, time of evaporation and frequency change observed on the deposition monitor (where a deposition monitor was used).

Evaporation	Pressure (μTorr)	Separation (cm)	Time (minutes)	Δf (Hz)	Thickness (μm)	Roughness (μm)
1	2.9 ± 0.1	5.0 ± 0.5	5	-	$6\mu m$	1.3
2	1.5 ± 0.1	5.0 ± 0.5	25	-	$2.5\mu m$	0.65
3	8.8 ± 0.1	7.0 ± 0.5	160	3318	$0.57^{+0.09}_{-0.05}$	0.40
4	3.0 ± 0.1	7.0 ± 0.5	160	4048	$0.77^{+0.07}_{-0.06}$	0.50
5	6.6 ± 0.1	15.5 ± 0.5	120	27933	$0.79^{+0.05}_{-0.06}$	0.11
6	6.8 ± 0.1	15.5 ± 0.5	120	31857	$0.91^{+0.11}_{-0.07}$	0.15

The objectives of the experiment were to produce TPB deposits that were $0.9\mu m$ thick on average, with no more than $0.3\mu m$ variation across the surface of the slide. From the final test evaporation it is clear this was achieved, with room to spare in terms of the variation observed. This is excellent, as the scans taken on the outer smaller removable discs were not right at the edge of the TPB deposit, so this leaves room for the continued decrease in deposition thickness that would be expected across the very edge of the slide. Due to the limitations of the AFM, this could not be confirmed, but given the conformation of observed distributions with theoretical distribution models, we can be confident that the deposit thicknesses produced were within allowed parameters.

The final settings for producing the required thickness of TPB deposit was deduced to be a crucible to slide separation of 15.5 ± 0.5, heating wire settings of $4.0 \pm 0.2V$ and $0.42 \pm 0.02A$ and a pressure of $\sim 7 \times 10^{-6} Torr$. The evaporation process should be left at these settings for approximately 2 hours to produce a frequency change of $31800Hz$ on a deposition monitor mounted next to the slide optical mount, with its surface at the same height as the slide surface. These settings were used to produce the final TPB deposits on the sanded acrylic and should be replicated in any future evaporations.

The deposition monitor was very successful in facilitating a slow, smooth evaporation. The limitations on resolution with the AFM meant that calibrating the frequency change to height thickness was not as accurate as may have been desired, but it was sufficient for the purposes of these evaporations. The AFM in general was not an ideal means of measuring the topographic thickness. The problem of having only a small $75\mu m$ square window to scan, and no means of calibrating where exactly you were on the surface of the slide whilst performing the scan, other than by eye through the side of the microscope, limited the ability to look at the complete distribution across the slide. It would have been nice to have taken multiple readings at many more different places to get a clearer sense of the distribution.

The cling film strips worked well in producing a TPB to no TPB step that would fit within the AFM scan window, but it is not known how much of the variation observed in step height is actually due to the disturbance caused by the cling film removal, distortions in the AFM calibration, or an actual feature of the TPB deposit. There was certainly a

lot of damage to the edge in places, making it impossible to land the AFM tip on the surface. However, attempts at cutting a line through the TPB surface with a fine scalpel generated even more surface damage, so given the equipment available, the cling film was the better option. It was also very beneficial to be able to map the topography of the TPB using the AFM, even over such small areas. It meant we had a clear indication that depositions were smoother and forming a more uniform layer.

Increasing the distance between the crucible and the slide definitely made a significant different to the distribution across the surface, massively reducing the variation in height. It would be interesting to try evaporating with a crucible with a larger opening to see if this could be improved even further. However, in doing so it is important that the heating process remains uniform throughout the crucible to ensure an even distribution. The final separation of 15.5 ± 0.5 was the maximum allowable space inside the evaporator in the Invisibles Lab, but if we had access to a larger evaporator somewhere on campus, it may be possible to reduce the effect of the evaporation distribution even further. However, as it stands the distribution was reduced sufficiently to fall within the desired variation, so at this stage there seems no need to pursue this further.

Overall these evaporations were successful in producing the required thickness TPB deposits, and a well controlled system and apparatus set-up is in place to replicate it as needed in the future to produce more slides of exactly the same depth and smoothness.

3 DEAP-3600 sensitivity plots

3.1 Modelling the WIMP-nucleon interaction

The differential energy spectrum for WIMP recoil is a complex model that incorporates form factors, spin- dependent and spin-independent interactions and many other astrophysical and particle physics variables. In this section I will attempt to work through the steps for deriving this model in the specific context of the DEAP-3600 liquid Argon experiment, which is sensitive to spin-independent WIMP-nucleus interactions. All major steps will be, as much as possible, derived from first principles, with motivations and justifications throughout. However, there are some parts of the calculation - particularly the form factor and detector response function - that are beyond the scope of this project. The motivation for these choices are therefore only briefly sketched out.

The entirety of the following calculations are detailed in R.W. Schnee's *Introduction to Dark Matter Experiments* [39] and in considerably more depth in Lewin and Smith's *Review of mathematics, numerical factors, and corrections dark matter experiments based on elastic nuclear recoil* [1].

3.2 Recoil energy

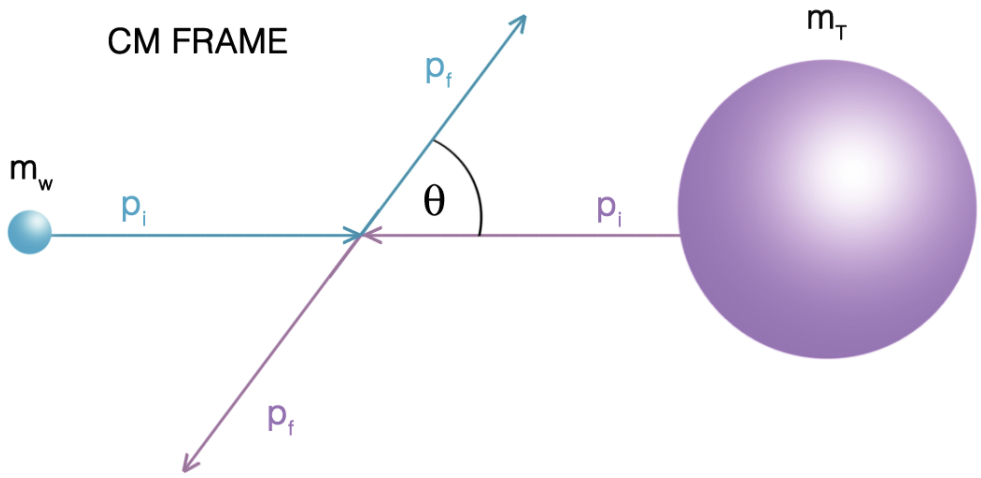

Figure 36: A collision between the dark matter WIMP and the Argon target nuclei in the centre of momentum frame where their momenta are equal and opposite.

The collision between the dark matter particle and the target Argon nuclei is modelled as an elastic scattering in two dimensions. Dark matter particles are cold so we can use non-relativistic dynamics in the centre of mass frame where the momentum of the dark matter particle and the target particle are equal and opposite before and after the collision. If the mass of the WIMP is m_w, the mass of the target is m_T and the velocity of the WIMP is v, then the velocity of the centre of momentum frame is

$$v_c = \frac{m_w v_w}{m_w + m_T}$$

Using right on the diagram above as the positive direction, the momentum of the target nuclei in the centre of momentum frame can be expressed as

$$p_i^T = -m_T v_c = -\frac{m_T m_w v_w}{m_w + m_T}$$

Because the momentum of the WIMP must be equal and opposite in this frame we know

$$p_i^w = \frac{m_T m_w v_w}{m_w + m_T}$$

We now need to calculate the energy that is transferred from the WIMP to the target nucleus during this collision in the lab frame. This can be done by resolving the lab frame velocity of the target nucleus after collision into horizontal and vertical components that depend on the angle of scattering, θ. First, in the centre of mass frame the velocity components are

$$v_x^{Tc} = v_c cos(\theta) \qquad \text{(horizontal velocity component)}$$
$$v_y^{Tc} = v_c sin(\theta) \qquad \text{(vertical velocity component)}$$

To find the target nuclei velocity in the lab frame, we simply remove the centre of mass velocity from the horizontal (x) velocity component. The transverse (y) velocity will be the same in both frames.

$$v_x^{Tc} = v_c cos(\theta) - v_c$$
$$v_y^{Tc} = v_c sin(\theta)$$

Using these we can then calculate what the kinetic energy of the target nucleus after the collision will be.

$$E_T = \frac{1}{2} m_T v_T^2$$
$$v_T^2 = (v_x^{Tc})^2 + (v_y^{Tc})^2$$
$$E_T = \frac{1}{2} m_T ((v_x^{Tc})^2 + (v_y^{Tc})^2)$$
$$E_T = \frac{1}{2} m_T \left(v_c^2 (cos(\theta) - 1)^2 + v_c^2 sin^2(\theta) \right)$$
$$\begin{aligned}(cos(\theta) - 1)^2 + sin^2(\theta) &= cos^2(\theta) + 1 - 2cos(\theta) + sin^2(\theta) \\ &= 2 - 2cos(\theta) \\ &= 2(1 - cos(\theta))\end{aligned}$$
$$E_T = \frac{1}{2} m_T v_c^2 \left(2(1 - cos(\theta))\right.$$
$$E_T = m_T v_c^2 (1 - cos(\theta))$$
$$E_T = m_T \frac{m_w^2 v_w^2}{(m_T + m_w)^2} (1 - cos(\theta)).$$

This is the recoil energy of the target nucleus, which we want to express in terms of the incoming energy of the WIMP particle E_w which will be

$$E_w = \frac{1}{2} m_w v_w^2$$

$$2E_w = m_w v_w^2.$$

Substituting this into the equation for the recoil energy we arrive at

$$E_T = 2E_w \frac{m_T m_w}{(m_T + m_w)^2}(1 - cos(\theta)).$$

This simplifies by introducing a kinematic factor, r, defined as

$$r = \frac{4 m_T m_w}{(m_T + m_w)^2}$$

so the recoil energy becomes

$$E_T = \frac{E_w r}{2}(1 - cos(\theta)).$$

If we assume the scattering is isotropic, i.e. uniform in $cos(\theta)$ between -1 and 1, then the recoil energies of the target nucleus, E_T, are uniformly distributed over the range $0 \leq E_T \leq E_w r$. We can then express the differential of the interaction rate in terms of the energy as

$$\frac{\mathrm{d}R}{\mathrm{d}E_T} = \int_{E_{min}}^{E_{max}} \frac{1}{E_w r} \, \mathrm{d}R(E).$$

Here the smallest possible WIMP particle energy that can cause the target to recoil is E_{min}, which will be E_T/r. The mean dark matter energy E_0 corresponds to the mean particle velocity v_0 defined as

$$E_0 = \frac{1}{2} m_w v_0^2 = \left(\frac{v_0^2}{v_w^2} \right) E_w.$$

We can then rearrange this to sub into the above integral to switch from energy to velocity as follows:

$$E_w = \frac{v_w^2}{v_0^2} E_0$$

$$\frac{\mathrm{d}R}{\mathrm{d}E_T} = \frac{1}{E_0 r} \int_{v_{min}}^{v_{max}} \frac{v_0^2}{v_w^2} \, \mathrm{d}R(v).$$

Now we have an expression for the differential event rate with changing recoil energy of the target nucleus, as a function of the mean velocity and energy of the dark matter of in our galaxy, and the actual velocity of the WIMP in this particular collision. We now need to see how the event rate behaves as a function of the WIMP velocity to find an expression for $dR(v)$.

3.3 Event rate

The event rate, R, per unit mass of dark matter scatterings off target nuclei of atomic mass A, with cross-section per nucleus σ will be

$$\mathrm{d}R(v) = \frac{N_0}{A} \sigma v \, \mathrm{d}n.$$

where v is the dark matter velocity, dn is the differential dark matter particle number density and N_0 is Avogadro's constant. Here we will first consider the case of zero momentum transfer, so the WIMP-nucleus cross-section is a constant, σ_0. The motivation for this choice will become clear later. It should also be noted that this WIMP-nucleus cross-section can be expressed in terms of the WIMP-nucleon cross section, σ_n, using

$$\sigma_0 = \sigma_n \frac{\mu_N^2}{\mu_n^2} A^2$$

where μ_N and μ_n are the reduced masses of the WIMP-nucleus and WIMP-nucleon systems respectively, defined as:

$$\mu_N = \frac{m_w m_N}{m_w + m_N} \qquad\qquad \mu_n = \frac{m_w m_n}{m_w + m_n}$$

where m_w is the mass of the WIMP, m_N is the mass of the nucleus and m_n is the mass of the nucleon.

The dark matter particle number density can be expressed as

$$\mathrm{d}n = \frac{n_0}{k} f(v_w, v_E) \mathrm{d}^3 v$$

where n_0 is the mean dark matter particle density in our galaxy (ρ_w / m_w) and $f(v, v_E)$ is the dark matter velocity distribution. We assume a Maxwellian distribution, which is a function of the colliding WIMP's individual velocity v_w and the velocity of the Earth v_E relative to the incoming dark matter particle.

$$f(v_w, v_E) = \exp\left(-\frac{(v_w + v_E)^2}{v_0^2}\right)$$

The k in the equation for the particle number density is a normalisation constant which ensures

$$\int_0^{v_{esc}} \mathrm{d}n = n_0.$$

If we substitute in the actual equations we find

$$k = \int_0^{v_{esc}} f(v_w, v_E)\, \mathrm{d}^3 v$$

where v_{esc} is the local Galactic escape velocity.

$$k = \int_0^{2\pi} \mathrm{d}\phi \int_0^{\pi} sin(\theta)\, \mathrm{d}\theta \int_0^{v_{esc}} v^2 f(v_w, v_E)\, \mathrm{d}v$$

$$k = 4\pi \int_0^{v_{esc}} \exp\left(-\frac{(v_w + v_E)^2}{v_0^2}\right) \mathrm{d}v.$$

This integral can be performed up to various different escape velocities. It is simplest to leave k in as a constant, and express the rate as a function of k and k_0, which is the result when you integrate between 0 and $v_{esc} = \infty$. This integral gives $k_0 = \pi^{\frac{3}{2}} v_0^3$. See Appendix A for the details of this integration, which is quite lengthly.

Before putting these results back into the equation for the event rate per unit mass, it is useful to define a new quantity R_0

$$R_0 = \frac{2}{\pi^{\frac{1}{2}}} \frac{N_0}{A} \frac{\rho_w}{m_w} \sigma_0 v_0$$

We can then write R as

$$R(v) = R_0 \frac{k_0}{k} \frac{1}{2\pi v_0^4} \int v_w f(v_w, v_E)\, \mathrm{d}^3 v$$

or in differential form

$$\mathrm{d}R(v) = R_0 \frac{k_0}{k} \frac{1}{2\pi v_0^4} v_w f(v_w, v_E)\, \mathrm{d}^3 v$$

This can now be substituted into the equation for the differential event rate

$$\frac{\mathrm{d}R}{\mathrm{d}E_T} = \frac{R_0}{E_0 r} \frac{k_0}{k} \frac{1}{2\pi v_0^2} \int_{v_{min}}^{v_{max}} \frac{1}{v_w} f(v_w, v_E)\, \mathrm{d}^3 v.$$

The simplest case is when $v_{max} = \infty$. The details of performing this integral between v_{min} and ∞ can be found in Appendix B. The result is reproduced below.

$$\frac{\mathrm{d}R}{\mathrm{d}E_T} = \frac{R_0}{E_0 r} \frac{\pi^{\frac{1}{2}}}{4} \frac{v_0}{v_E} \left[\mathrm{erf}\left(\frac{v_{min} + v_E}{v_0} \right) - \mathrm{erf}\left(\frac{v_{min} - v_E}{v_0} \right) \right].$$

Most of the remaining variables (including those contained within R_0) are known quantities, such as the mass of the target, m_T, or can be estimated using astrophysical constraints, such as the WIMP wind velocity, v_0, and local dark matter density, ρ_0. That leaves the mass and cross section of the WIMP. The differential rate is plotted below as a function of the nuclear recoil energy for an assumed WIMP cross section of $10^{-45} cm^2$ and various different potential WIMP masses.

If we assume the event rate is Poisson distributed, i.e. there is a 10% probability to see 0 events with a mean number of events of 2.3, then we can integrate this plot for a given mass, and then rearrange for the corresponding cross section. The integration needs to be performed over the target energy recoil threshold window DEAP-3600 is capable of detecting. The current predicted threshold background limit (based on projected background subtraction results from DEAP-1) is to recoil energies as low as $15 keVee$ [40] with a window of around 25keVee. Here the unit is expressed in terms of the electron-equivalent energy. If this integration is performed for a range of possible WIMP masses, it is possible to plot the range of WIMP dark matter cross sections and corresponding masses that the DEAP-3600 experiment will be sensitive to.

3.4 Nuclear form factor

Up until this point it has been assumed that there is zero momentum transfer in this WIMP-nucleon interaction, because the underlying physical nature of such an interaction is unknown, and thus the predicted momentum transfer, q is unknown. However, the nature of the dark matter-WIMP interaction is of vital importance in modelling the predicted sensitivity of DEAP-3600, so it is therefore necessary to introduce a theoretical momentum transfer model term that can be applied to the zero-momentum transfer case. Such a term is known as a form factor, as it applies the required "form" observed in measurements without a need to know or understand the underlying physics of the process being described.

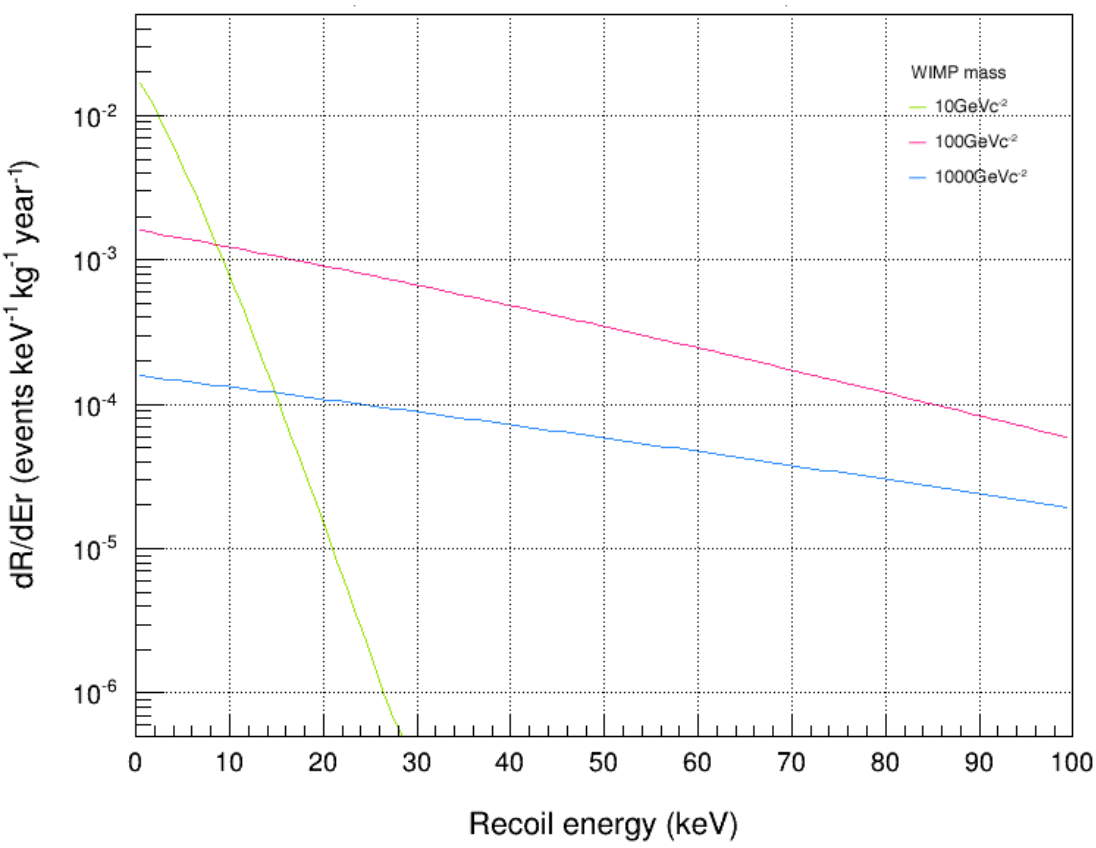

Figure 37: Differential event rate as a function of WIMP-induced nuclear recoil energy in liquid argon for an assumed WIMP interaction cross section of $10^{-45} cm^{-2}$ and three different possible WIMP masses.

Thus the cross section for the interaction can be modelled using the previously assumed zero momentum transfer σ_0 and the form factor, F as

$$\sigma = \sigma_0 F^2.$$

It has been experimentally observed that in scattering interactions of the type assumed here (where the wavelength h/q is not large compared to the nuclear radius), the effective cross section becomes smaller with increasing momentum transfer. The form factor required is thus a dimensionless function of the momentum transfer, $qr_n/\hbar$, where r_n is the nuclear radius, which can be expressed as

$$r_n = a_n A^{\frac{1}{3}} + b_n$$

where A is the atomic number of the target and a_n and b_n are constants with the dimensions of length. The momentum transfer in $MeVc^{-1}$ can thus be expressed as

$$q = (2m_T E_T)^{\frac{1}{2}} = (2 \times 0.932\ [GeVc^{-2}]\ A\ E_T[keV])^{\frac{1}{2}}.$$

Then to make the function dimensionless we set $\hbar$, which is $197.3 MeV fm$, to 1, to use natural units, and produce the function

$$qr_n = 6.92 \times 10^{-3}(AE_R[keV])^{\frac{1}{2}}(a_n[fm]A^{\frac{1}{3}} + b_n[fm]).$$

As mentioned earlier, the exact nature of the form factor is determined from experiment, and for the spin-independent case that DEAP-3600 is sensitive to, the scattering distribution is assumed to be much like that for electron and muon scattering. These form factors are an area of current active research, and many fits have been proposed. For the purposes of this model, the Helm Form Factor [41] has been adopted, as it takes the (fairly) straightforward analytical form

$$F = 3\left(\frac{sin(qr_n)}{(qr_n)^3} - \frac{cos(qr_n)}{(qr_n)^2}\right)e^{\frac{-(qs)^2}{2}}$$

where s is defined as the "skin" thickness. This accounts for the nucleus being modelled as a solid sphere with a soft edge where the charge density rapidly falls to zero, effectively damping recoil response.

The unknown values in this form factor are all dependent on the target nucleus, and will therefore be constants of the experiment. Fitting to muon scattering data yields commonly used approximations for these constants of $a_n = 1.14fm$ and $b_n = 0fm$. For the skin thickness, Lewin & Smith suggest $s = 0.9fm$ provides the best fit to both the Helm factor and a numerically integrated Fermi distribution [1].

3.5 Detector response

A remaining factor to be considered in this model is that so far we have assumed that our detector is 100% efficient at detecting every interaction that occurs. In practice this cannot be the case. There will be considerable quenching of the energy imparted by the in coming WIMP due, predominantly, to electrons recombining before forming the scintillation excimers. Additionally, the 255 8-inch Hamamatsu R5912 HQE PMTs detecting the scintillation light have a quantum efficiency of just 32%, and 75% coverage of the target body, so even if all the energy imparted was converted to scintillation light, not all events will be detected.

The detector response compensation code used for this model was written by Mark Boulay at Queen's University in Canada based on projections from DEAP-1 data. The recoil energy quenching factor is taken at 0.25 of the total energy [40]. The detector energy resolution is then fitted with a second order polynomial with experimentally determined constant parameters. The final energy detected for any single given energy will take the form of an approximately Gaussian spectral distribution. All of these contributions are applied to the event rate, along with the nuclear form factor, to produce a measured energy distribution for DEAP-3600. It is this plot that is then integrated between the threshold energy window to calculate the cross section for a given WIMP mass.

3.6 Mass vs cross section plot

A code was written in ROOT to calculate and plot the mass vs cross section for the DEAP-3600 sensitivity. The code was developed with assistance from scripts by Mark

Boulay. The finished code can be found in Appendix C, and the resulting plot is shown below for the following variables:

E_{thresh}	$15keVee$	Energy threshold of detector
E_{window}	$25keVee$	Energy window of detector
m_T	$1000kg$	Mass of the target in the detector
$quench$	0.25	Recoil quenching factor
ρ_0	$0.3GeVc^{-2}cm^{-3}$	WIMP density
v_0	$220kms^{-1}$	WIMP wind velocity
v_e	$244kms^{-1}$	Earth velocity
t	$94672800s$	3 year exposure time

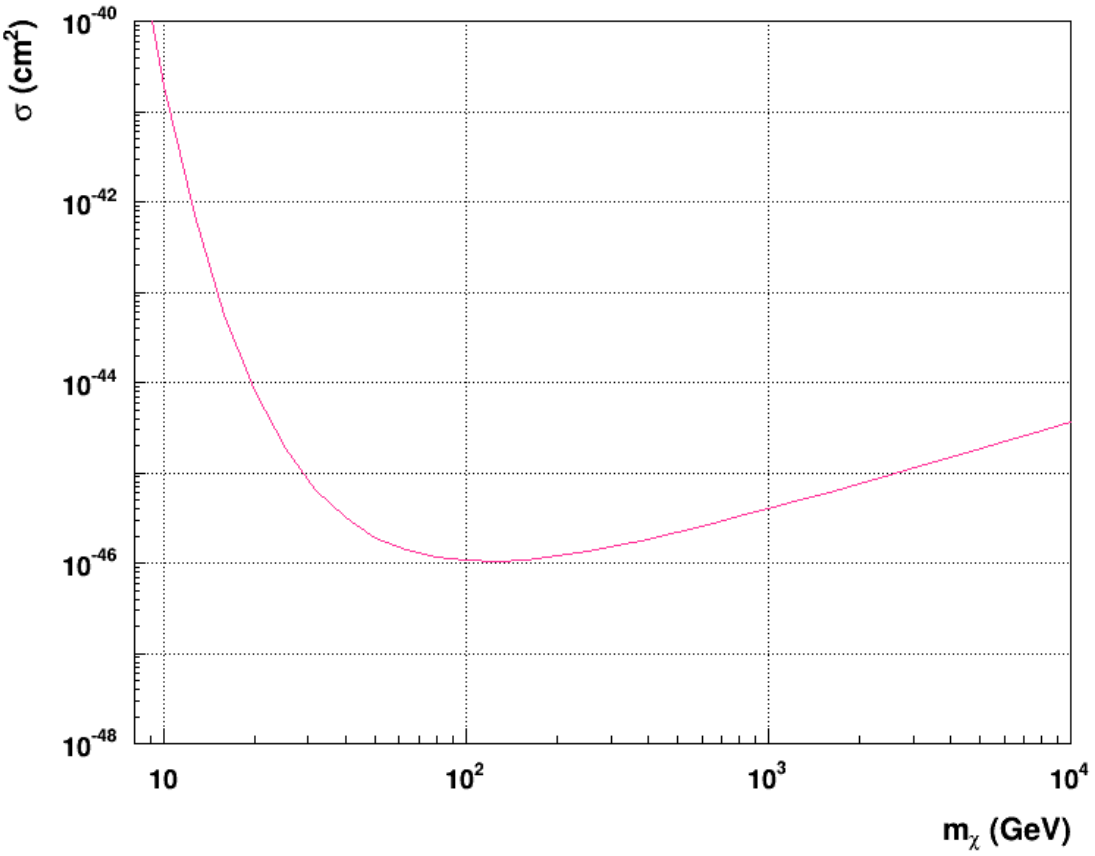

Figure 38: Sensitivity plot showing the limits of WIMP mass and interaction cross section combinations that will be detectable in DEAP-3600, assuming 2.3 events in 3 years running time. This shows a maximum sensitivity at $100GeV$ of $1 \times 10^{-46}cm^2$.

Everything above the line on this plot is a WIMP mass and cross section combination that DEAP-3600 should be sensitive to and be capable of detecting. The line itself marks the limit of this sensitivity, and everything beneath it will be unmeasurable. The range of potential dark matter masses plotted constitutes the allowed range based on astrophysical constraints. We can see that DEAP-3600 will have a maximum sensitivity at a WIMP mass of $100GeV$ and cross section of $1 \times 10^{-46}cm^2$. When the detector is up and running, this will make DEAP-3600 the most sensitive WIMP dark matter

experiment to date, overtaking the current best limit of $7.6 \times 10^{-46} cm^2$ at a WIMP mass of $33 GeV$, set by LUX liquid Xenon experiment in 2013. DEAP's sensitivity plot is overall shifted towards the higher mass region, so will also be more sensitive across the currently favoured higher mass WIMP's of between 100 and $1000 GeV$.

These plots are used by researchers working on dark matter direct detection experiments to compare the sensitivity of different experimental techniques, in the quest to carve down into this mass-cross section parameter space, hunting for a signal that indicates the presence of dark matter. There have been several claims of positive dark matter direct detection from groups such as DAMA/LIBRA [16], but these regions have subsequently been ruled out by other direct detection experiments probing the same regions [15]. Thus, these plots provide a vital tool for balances and checks across scientific groups in the dark matter direct detection field. It is therefore very important that the assumptions we have made for various parameters accurately reflect the best predicted values.

3.7 Varying parameters

The WIMP wind velocity here has been set for this model at an average of $220 kms^{-1}$ and the velocity of the Earth at $244 kms^{-1}$. However, it is considered a key identifier of dark matter direct detection that the WIMP wind velocity should change across the course of the year [42]. The WIMP wind is caused by the solar system's motion around the galaxy, pulling us through the dark matter halo. So, in reality it is us that is moving, not the dark matter, but we experience the results of this motion as a dark matter flux relative to our own motion.

The annual variation is observed because as the Earth orbits around the sun it is sometimes moving "upstream" to the WIMP wind velocity, and sometimes "downstream". This means the Earth's velocity relative to the dark matter velocity changes, adding constructively or destructively to alter the resultant dark matter flux experienced. As a consequence, we expect to see a noticeable shift in the energy spectrum of incoming WIMPs as they pass through the detector, which means the sensitivity will change at different times of year.

The maximum relative Earth velocity will occur on June 1 or 2, when it is estimated to be as much as $258 kms^{-1}$ due to the Earth moving in its orbit around the sun in the same direction as the motion of the solar system around the galaxy. It is estimated to be a minimum of $229 kms^{-1}$ on December 3 or 4, when the Earth's orbit moves it in the opposite direction to the solar system [1].

The effect of this variation on the differential rate plot and the sensitivity plot for DEAP-3600 can be seen below, with plots for the maximum, minimum and average Earth velocities across the year. It is clear this effect results in a measurable change, which over the 3 year DEAP-3600 running time, would be visible. However, the caveat of using this modulation as an indicator for dark matter is that the annual modulation amplitude falls on top of a very large amount of background, so the statistical methods for extracting evidence from the measurements can be problematic [43]. Comprehensive background subtraction is therefore vital to confirm the observation of a varying dark matter flux.

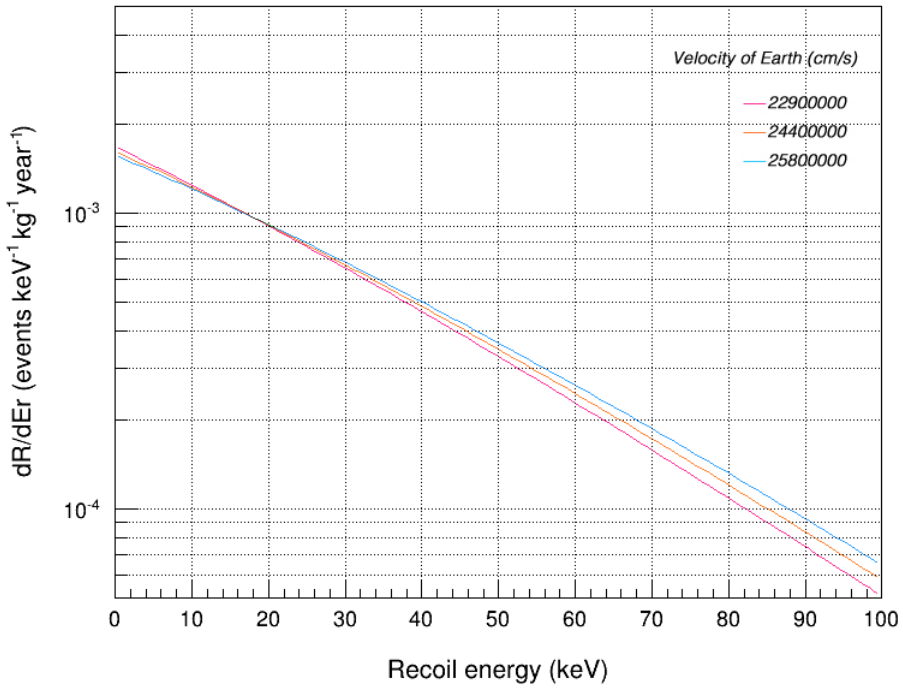

Figure 39: Differential event rate as a function of nuclear recoil energy in liquid argon for a WIMP mass of $100GeVc^{-2}$ and a cross section of $10^{-45}cm^{-2}$ with different Earth velocities.

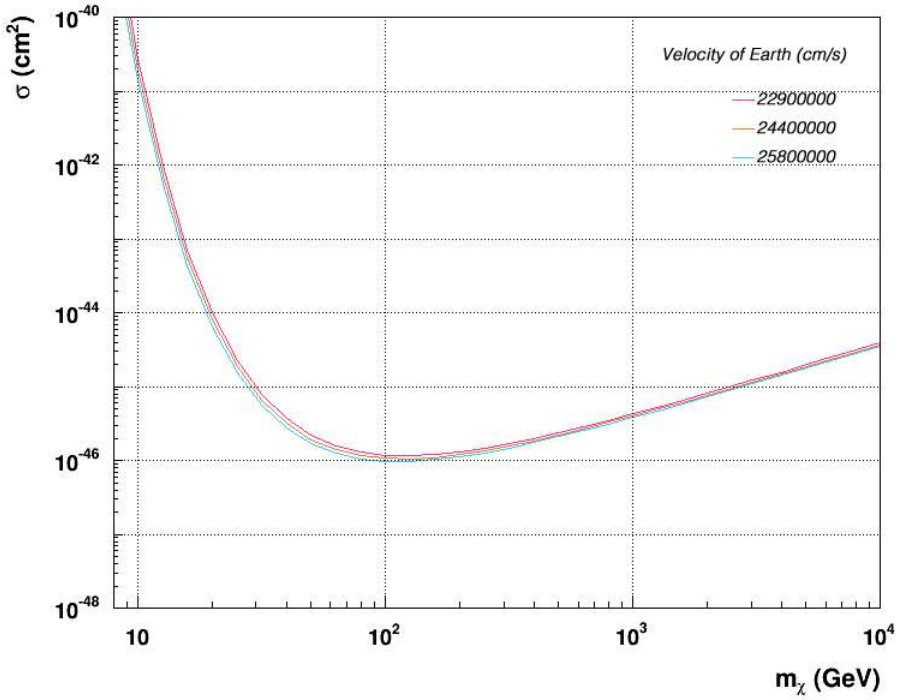

Figure 40: DEAP-3600 dark matter sensitivity plot changing the Earth's velocity to the minimum, average and maximum velocities it achieves across the course of the year due to its orbit around the sun. We can see the experiment will be the most sensitive in June, when the Earth's velocity is a maximum.

The energy threshold and window are determined from projections based on DEAP-1 measurements, so cannot be fully established until the detector is up and running. As a consequence, these parameters too, could change and the range of energies the detector is capable of reading will, of course, influence it's sensitivity considerably. The plots below show changes to both the position of the energy window, and the size of the energy window to see how it will effect the overall sensitivity.

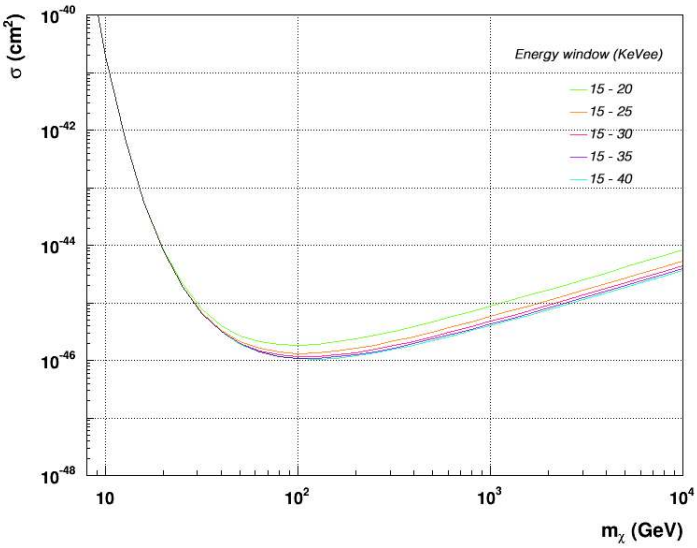

Figure 41: DEAP-3600 dark matter sensitivity plot keeping the same lower energy threshold of 15keVee, but changing the size of the energy window.

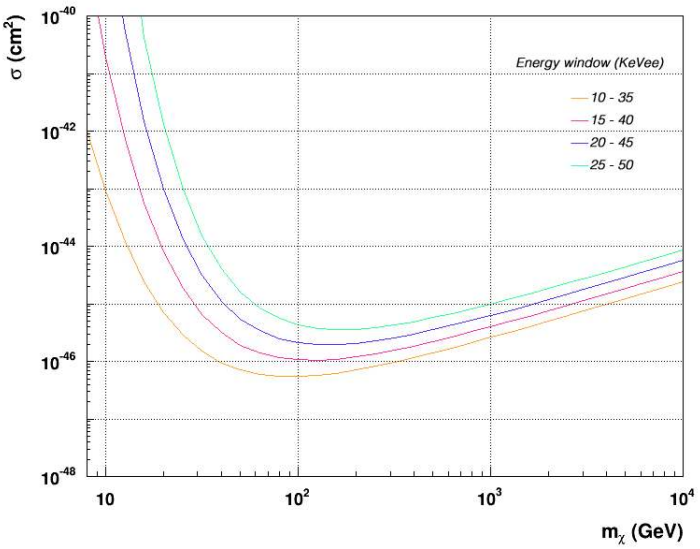

Figure 42: DEAP-3600 sensitivity plot with the energy window kept at 25keVee, but moved higher and lower in the energy distribution.

3.8 Conclusions

4 Conclusion

5 References

[1] Lewin, J.D. and Smith, P.F., *Review of mathematics, numerical factors, and corrections for dark matter experiments based on elastic nuclear recoil*. Astroparticle Physics 6, 87-112 , 1996

[2] Ade, P. A. R.; Aghanim, N.; Armitage-Caplan, C.; et al. (ESA/Planck, and the Planck Collaboration) *Planck 2013 results. I. Overview of products and scientific results*, Astronomy and Astrophysics manuscript no. PlanckMission2013, arXiv:1303.5062 [astro-ph.CO], 20 March 2013

[3] Fuchs, B. *The amount of dark matter in spiral galaxies*, arXiv:astro-ph/0010358, 2000

[4] Salucci, P. and Persic, M. *Dark matter halos around galaxies* ASP Proceedings Conference Series 1997, arXiv:astro-ph/9703027

[5] Garrett, K. and Duda, G. *Dark Matter: A Primer* Adv.Astron.2011:968283,2011, arXiv:1006.2483

[6] Lippincott, W.H. *Direct detection of dark matter with liquid argon and neon*, Yale University, 2010

[7] Bertone, G., Hooper, D. and Silk, J. *Particle Dark Matter: Evidence, Candidates and Constraints*, Phys.Rept.405:279-390, arXiv:hep-ph/0404175 2005

[8] Cushman, P. Galbaiti, C., McKinsey, D.N. et al; *Snowmass CF1 Summary: WIMP Dark Matter Direct Detection*, Community Planning Study: Snowmass 2013 arXiv:1310.8327 [hep-ex]

[9] Jungman, G.; Kamionkowski M.; Griest, K. *Supersymmetric dark matter*Physics Reports, Volume 267, Issues 56, March 1996, Pages 195-373

[10] Abazajian, K., Fuller, G.M. and Patel, M. *Sterile Neutrino Hot, Warm, and Cold Dark Matter*. Phys.Rev. D64 (2001) 023501, arXiv:astro-ph/0101524

[11] Duffy, L.D. and Bibber, K. *Axions as Dark Matter Particles*, New J.Phys.11:105008,2009, arXiv:0904.3346 [hep-ph]

[12] Hsin-Chia Cheng, Jonathan L. Feng, Konstantin T. Matchev *Kaluza-Klein Dark Matter*, Phys.Rev.Lett.89:211301,2002, arXiv:hep-ph/0207125

[13] Tait, T. Hooper, D. *Theories of particle dark matter* Comptes Rendus Physique, Volume 13, Issues 67, JulySeptember 2012, Pages 719-723

[14] Figueroa-Feliciano, E. *Direct detection searches for WIMP dark matter*. Progress in Particle and Nuclear Physics 66 (2011) 661673

[15] Akerib,D.S.; Araujo, H.M.; Bai, X.; et al. *First results from the LUX dark matter experiment at the Sanford Underground Research Facility*. Phys. Rev. Lett. 112, 091303, arXiv:1310.8214, 2014

[16] Bernabei, R.; Belli, P.; F. Cappella, F.; et al. *New results from DAMA/LIBRA*. European Physics. J. C 67: 39-49, arXiv:1002.1028 [astro-ph.GA], 2010

[17] Aalseth, C.E., Barbeau,P.S., Colaresi J. et al; *Search for an Annual Modulation in a P-type Point Contact Germanium Dark Matter Detector*, Phys. Rev. Lett. 107 141301, 2011

[18] Walding, J. *The DEAP search for dark matter*. IOP HEPP APP 2014, Royal Holloway, University of London, 8th April 2014

[19] *SNOLAB Users Handbook*, `http://snolab2008.snolab.ca/snolab_users_handbook_rev02.pdf`

[20] Heusser, G. *Low-Radioactivity Background Techniques*. Annual Review of Nuclear and Particle Science Vol. 45 (1995): 543-590

[21] Chapel,V. and Araujo, H. *Liquid noble gas detectors for low energy particle physics* . 2013 JINST 8 R04001, arXiv:1207.2292 [physics.ins-det], 2013

[22] Galbiati, C., Purtschert, R., et. al *Discovery of underground argon with low level of radioactive* ^{39}*Ar and possible applications to WIMP dark matter detectors* J.Phys.Conf.Ser.120:042015,2008, arXiv:0712.0381 [astro-ph]

[23] Pollmann, T. *Alpha Backgrounds In The DEAP Dark Matter Search Experiment*, Thesis submitted to the Department of Physics, Engineering Physics and Astronomy, Queen's University, Kingston, Ontario, Canada, June 2012

[24] Doke, T.; Hitachi, A.; Kikuchi, J. et al; *Absolute Scintillation Yields in Liquid Argon and Xenon for Various Particles* Jpn. J. Appl. Phys. Vol. 41 (2002) pp. 15381545

[25] Kubota, S., Hishida, M. and Raun, J. *Evidence for a triplet state of the self-trapped exciton states in liquid argon, krypton and xenon*, J. Phys. C: Solid State Phys. 11 (1978) 2645.

[26] Kima, J.H.; Noha, S.; Kimb, K.; et al; *Blue light emitting diode with 1,1,4,4-tetraphenyl-1,3-butadiene (TPB)* . Synthetic Metals, Volume 117, Issues 13, 15 February 2001, Pages 227-228

[27] Lally, C.H.; Davies, G.J.; Jones, W.G.; et al. *UV quantum efficiencies of organic fluors* Nuclear Instruments and Methods in Physics Research B 117 421-427, 1996

[28] Wehry, E.L.; Editor Settle, F.A.; *Handbook of Instrumental Techniques for Analytical Chemistry: Chapter 26: Molecular Fluorescence and Phosphorescence Spectrometry.* Prentice Hall, US, 1997

[29] Berlman, X. *Handbook of Fluorescence Spectra of Aromatic Molecules.* 2nd Ed. (Academic Press, New York).

[30] Burton, W.M. and Powell, B.A.*Fluorescence of TetraPhenyl-Butadiene in the Vacuum Ultraviolet,*, Appl. Opt., 12, 87, 1973

[31] Gehman V.M.; Seibert, S.R.; Rielage, K., et al. *Fluorescence efficiency and visible re-emission spectrum of tetraphenyl-butadiene films at extreme ultraviolet wavelengths* Nucl. Instr. and Meth. A654, 116, arXiv:1104.3259 [astro-ph.IM], 2011

[32] Hamamatsu *Large Photocathode Area Photomultiplier Tubes.* Technical specifications, 2008

[33] Flournoy, J. M., Berlman, I. B., Rickborn, B. et al, *Substituted tetraphenylbutadienes as fast scintillator solutes*, Nucl. Instrum. Meth. A 351 349, 1994

[34] Davies, G.J.; Lally, C.H.; Jones, W.G.; et al. *UV quantum efficiencies of organic fluors.* Nuclear Instruments and Methods in Physics Research Section B, 117:421, 1996.

[35] McKinsey, D.N.; Brome, C.R.; Butterworth, J.S.; et al. *Fluorescence efficiencies of thin scintillating films in the extreme ultraviolet spectral region.* Nuclear Instruments & Methods In Physics Research Section B-Beam Interactions With Materials And Atoms, 132(3):351358, 1997

[36] Sigma-Aldrich *Material Safety Data Sheet - TPB.* Technical report, 2010.

[37] Chiu, C.; Ignarra, C.; Bugel, L., et al. *Environmental Effects on TPB Wavelength-Shifting Coatings.* arXiv:1204.5762 [physics.ins-det], 2012

[38] Jerry, R.; Winslow, L. Bugel, L., et al. *A Study of the Fluorescence Response of Tetraphenyl-Butadiene.* arXiv:1001.4214 [physics.ins-det], 2010

[39] Schnee R.W., *Introduction to Dark Matter Experiments.* Physics of the Large and Small: Proceedings of the 2009 Theoretical Advanced Study Institute in Elementary Particle Physics, pp. 629-681 (World Scientific, Singapore), Ed. Csaba Csaki and Scott Dodelson, arXiv:1101.5205 [astro-ph.CO], 2010

[40] Boulay, M., *DEAP-3600 Dark Matter Search at SNOLAB.* Proceedings for the 12th International Conference on Topics in Astroparticle and Underground Physics, arXiv:1203.0604 [astro-ph.IM], 2011

[41] Helm, R.H., *Inelastic and Elastic Scattering of 187-Mev Electrons from Selected Even-Even Nuclei.* Physics Review 104, 1466, December 1956

[42] Drukier, A.K., Freese, K. and Spergel, D.N. *Detecting cold dark-matter candidates* Phys. Rev. D 33, 3495, June, 1986

[43] Freese, K., Lisanti, M. and Savage, C. *Annual Modulation of Dark Matter: A Review*, Reviews of Modern Physics, 85 (4). pp. 1561-1581, arXiv:1209.3339 [astro-ph.CO], 2013

6 Appendices

6.1 Appendix A

Calculating the particle number density normalisation constant, $k = k_0$ by integrating between 0 and $v_{esc} = \infty$.

$$k = \int_0^{2\pi} \mathrm{d}\phi \int_0^{\pi} sin(\theta)\,\mathrm{d}\theta \int_0^{v_{esc}} v^2 f(v, v_E)\,\mathrm{d}v$$

$$k_0 = \int_0^{2\pi} \mathrm{d}\phi \int_{-1}^{+1} \mathrm{d}(cos(\theta)) \int_0^{\infty} v^2 \exp\left(-\frac{(v+v_E)^2}{v_0^2}\right) \mathrm{d}v$$

For a moving Earth v_E, $(v+v_E)^2 = v^2 + v_E^2 + 2vv_E cos(\theta)$

$$k_0 = 2\pi \int_{-1}^{+1} \mathrm{d}(cos(\theta)) \int_0^{\infty} v^2 \exp\left(-\frac{v^2 + v_E^2 + 2vv_E cos(\theta)}{v_0^2}\right) \mathrm{d}v$$

$$k_0 = 2\pi \int_{-1}^{+1} \int_0^{\infty} v^2 \exp\left(-\frac{(v^2+v_E^2)}{v_0^2}\right) \exp\left(-\frac{2vv_E cos(\theta)}{v_0^2}\right) \mathrm{d}(cos(\theta))\,\mathrm{d}v$$

$$k_0 = 2\pi \int_0^{\infty} \left[v^2 \exp\left(-\frac{(v^2+v_E^2)}{v_0^2}\right)\left(-\frac{v_0^2}{2vv_E}\right) \exp\left(-\frac{2vv_E cos(\theta)}{v_0^2}\right)\right]_{-1}^{+1} \mathrm{d}v$$

$$k_0 = 2\pi \int_0^{\infty} v^2 \exp\left(-\frac{(v^2+v_E^2)}{v_0^2}\right)\left(-\frac{v_0^2}{2vv_E}\right)\left[\exp\left(-\frac{2vv_E}{v_0^2}\right) - \exp\left(\frac{2vv_E}{v_0^2}\right)\right] \mathrm{d}v$$

$$k_0 = 2\pi \int_0^{\infty} v^2 \left(-\frac{v_0^2}{2vv_E}\right)\left[\exp\left(-\frac{(v+v_E)^2}{v_0^2}\right) - \exp\left(-\frac{(v-v_E)^2}{v_0^2}\right)\right] \mathrm{d}v$$

$$k_0 = \frac{\pi v_0^2}{v_E} \int_0^{\infty} v \left[\exp\left(-\frac{(v-v_E)^2}{v_0^2}\right) - \exp\left(-\frac{(v+v_E)^2}{v_0^2}\right)\right] \mathrm{d}v$$

$$k_0 = \frac{\pi v_0^2}{v_E} \left[\int_0^{\infty} v \exp\left(-\frac{(v-v_E)^2}{v_0^2}\right) \mathrm{d}v - \int_0^{\infty} v \exp\left(-\frac{(v+v_E)^2}{v_0^2}\right) \mathrm{d}v\right]$$

Make substitutions $x = v - v_E$ and $y = v + v_E$.

$$k_0 = \frac{\pi v_0^2}{v_E} \left[\int_{-v_E}^{\infty} (x+v_E) \exp\left(-\frac{x^2}{v_0^2}\right) \mathrm{d}x - \int_{v_E}^{\infty} (y-v_E) \exp\left(-\frac{y^2}{v_0^2}\right) \mathrm{d}y\right]$$

$$k_0 = \frac{\pi v_0^2}{v_E} \Bigg[\int_{-v_E}^{\infty} x \exp\left(-\frac{x^2}{v_0^2}\right) \mathrm{d}x + \int_{-v_E}^{\infty} v_E \exp\left(-\frac{x^2}{v_0^2}\right) \mathrm{d}x - \int_{v_E}^{\infty} y \exp\left(-\frac{y^2}{v_0^2}\right) \mathrm{d}y + \int_{v_E}^{\infty} v_E \exp\left(-\frac{y^2}{v_0^2}\right) \mathrm{d}y\Bigg]$$

$$k_0 = \frac{\pi v_0^2}{v_E} \Bigg\{ \left[-\frac{v_0^2}{2} \exp\left(-\frac{x^2}{v_0^2}\right)\right]_{-v_E}^{\infty} + \left[\frac{v_E v_0}{2}\sqrt{\pi}\,\mathrm{erf}\left(\frac{x}{v_0}\right)\right]_{-v_E}^{\infty} - \left[-\frac{v_0^2}{2} \exp\left(-\frac{y^2}{v_0^2}\right)\right]_{v_E}^{\infty} + \left[\frac{v_E v_0}{2}\sqrt{\pi}\,\mathrm{erf}\left(\frac{y}{v_0}\right)\right]_{v_E}^{\infty} \Bigg\}$$

Use that $\exp(-\infty) = 0$, $\mathrm{erf}(\infty) = 1$ and $\mathrm{erf}(-\infty) = -1$.

$$k_0 = \frac{\pi v_0^2}{v_E}\left\{ \left[0 + \frac{v_0^2}{2}\exp\left(-\frac{v_E^2}{v_0^2}\right)\right] + \left[\frac{v_E v_0}{2}\sqrt{\pi} - \frac{v_E v_0}{2}\sqrt{\pi}\,\mathrm{erf}\left(-\frac{v_E}{v_0}\right)\right] - \left[0 + \frac{v_0^2}{2}\exp\left(-\frac{v_E^2}{v_0^2}\right)\right] + \left[\frac{v_E v_0}{2}\sqrt{\pi} - \frac{v_E v_0}{2}\sqrt{\pi}\,\mathrm{erf}\left(\frac{v_E}{v_0}\right)\right] \right\}$$

$$k_0 = \frac{\pi v_0^2}{v_E}\left\{ \frac{v_E v_0}{2}\sqrt{\pi}\left[1 - \mathrm{erf}\left(-\frac{v_E}{v_0}\right) + 1 - \mathrm{erf}\left(\frac{v_E}{v_0}\right)\right] \right\}$$

Use that $\mathrm{erf}(x) = -\mathrm{erf}(-x)$.

$$k_0 = \frac{\pi v_0^2}{v_E}\,\frac{v_E v_0}{2}\sqrt{\pi}\,2$$

$$k_0 = \pi^{\frac{3}{2}} v_0^3$$

6.2 Appendix B

Calculating the differential rate for the simplest case when $v_{max} = \infty$.

$$\frac{\mathrm{d}R}{\mathrm{d}E_T} = \frac{R_0}{E_0 r}\frac{k_0}{k}\frac{1}{2\pi v_0^2}\int_{v_{min}}^{v_{max}}\frac{1}{v_w} f(v, v_E)\,\mathrm{d}^3 v$$

If $v_{max} = \infty$, then $k_0 = k$, so those two terms cancel.

$$\frac{\mathrm{d}R}{\mathrm{d}E_T} = \frac{R_0}{E_0 r}\frac{1}{2\pi v_0^2}\int_0^{2\pi}\mathrm{d}\phi\int_{-1}^{+1}\mathrm{d}(cos(\theta))\int_{v_{min}}^{\infty} v\exp\left(-\frac{(v+v_E)^2}{v_0^2}\right)\mathrm{d}v$$

$$\frac{\mathrm{d}R}{\mathrm{d}E_T} = \frac{R_0}{E_0 r}\frac{1}{2\pi v_0^2}2\pi\int_{-1}^{+1}\int_{v_{min}}^{\infty} v\exp\left(-\frac{v^2 + v_E^2 + 2vv_E cos(\theta)}{v_0^2}\right)\mathrm{d}(cos(\theta))\,\mathrm{d}v$$

The $\mathrm{d}(cos(\theta))$ integration here is identical to the one in Appendix A, so here we skip to the same final result.

$$\frac{\mathrm{d}R}{\mathrm{d}E_T} = \frac{R_0}{E_0 r}\frac{1}{v_0^2}\int_{v_{min}}^{\infty} v\left(\frac{v_0^2}{2vv_E}\right)\left[\exp\left(-\frac{(v-v_E)^2}{v_0^2}\right) - \exp\left(-\frac{(v+v_E)^2}{v_0^2}\right)\right]\mathrm{d}v$$

$$\frac{\mathrm{d}R}{\mathrm{d}E_T} = \frac{R_0}{E_0 r}\frac{1}{2v_E}\int_{v_{min}}^{\infty}\left[\exp\left(-\frac{(v-v_E)^2}{v_0^2}\right) - \exp\left(-\frac{(v+v_E)^2}{v_0^2}\right)\right]\mathrm{d}v$$

Make substitutions $x = v - v_E$ and $y = v + v_E$.

$$\frac{\mathrm{d}R}{\mathrm{d}E_T} = \frac{R_0}{E_0 r}\frac{1}{2v_E}\left[\int_{v_{min}-v_E}^{\infty}\exp\left(-\frac{x^2}{v_0^2}\right)\mathrm{d}x - \int_{v_{min}+v_E}^{\infty}\exp\left(-\frac{y^2}{v_0^2}\right)\mathrm{d}y\right]$$

$$\frac{\mathrm{d}R}{\mathrm{d}E_T} = \frac{R_0}{E_0 r}\frac{1}{2v_E}\left\{\left[\frac{v_0}{2}\sqrt{\pi}\,\mathrm{erf}\left(\frac{x}{v_0}\right)\right]_{v_{min}-v_E}^{\infty} - \left[\frac{v_0}{2}\sqrt{\pi}\,\mathrm{erf}\left(\frac{y}{v_0}\right)\right]_{v_{min}+v_E}^{\infty}\right\}$$

$$\frac{\mathrm{d}R}{\mathrm{d}E_T} = \frac{R_0}{E_0 r}\frac{1}{2v_E}\frac{v_0}{2}\sqrt{\pi}\left\{\left[1 - \mathrm{erf}\left(\frac{v_{min}-v_E}{v_0}\right)\right] - \left[1 - \mathrm{erf}\left(\frac{v_{min}+v_E}{v_0}\right)\right]\right\}$$

$$\frac{\mathrm{d}R}{\mathrm{d}E_T} = \frac{R_0}{E_0 r}\frac{\pi^{\frac{1}{2}}}{4}\frac{v_0}{v_E}\left[\mathrm{erf}\left(\frac{v_{min}+v_E}{v_0}\right) - \mathrm{erf}\left(\frac{v_{min}-v_E}{v_0}\right)\right]$$

6.3 Appendix C: Recoil energy spectrum ROOT code

WIMP-induced nuclear recoil energy spectrum code.

```
#include "TH1.h"
#include "TObject.h"
#include "TF1.h"
#include "math.h"
#include "TTimeStamp.h"
#include "TMath.h"

void DEAPrate()
{
  //clear previous objects in directory
  delete gDirectory->FindObject("canvas");
  delete gDirectory->FindObject("histrate");

  // --------- create histogram
  TH1F * histrate = new TH1F("histrate","", 100, 0., 100.);

  /// --------- define variables
  Double_t c          = 2.99792458e10;  // speed of light in cm/sec
  Double_t c2         = c*c;            // speed of light squared
  Double_t A          = 40;          // nuclear target atomic number (g/mol)
  Double_t sigman     = 1e-45;        // WIMP-Nucleon cross-section (cm^2)
  Double_t rho0       = 0.3e9/(c*c);     // WIMP density in eV/cm^3
  Double_t vo         = 22000000.;     // WIMP wind velocity in cm/sec
  Double_t ve         = 24400000.;     // Earth velocity in cm/sec
  Double_t t          = 86400*365;     // 1 year in seconds
  Double_t pi         = TMath::Pi();     // pi
  Double_t m_N        = A*931.5e6/c2;    // Nucleus mass in eV
  Double_t m_n       = 931.5*1e6/c2;      // Nucleon mass in eV
  Double_t m_w    = 100*1e9/c2;    // wimp mass in eV
  Double_t avogadro = 6.0221413e+23;  // Avogadro's constant

  // --------- calculation

  //WIMP-nucleus cross-section, spin-independent
  Double_t sigma0 = A*A*sigman*pow(((m_N*m_w)/(m_N+m_w))/((m_n*m_w)/(m_n+
      m_w)),2);
  // Event rate/mass/time (g^-1 s^-1)
  Double_t Ro   = 2*avogadro*rho0*sigma0*vo/(sqrt(pi)*A*m_w);
  // Kinematic factor (unitless)
  Double_t r  = 4*m_N*m_w/pow((m_N+m_w),2);
  // Average WIMP energy in eV
  Double_t Eo   = (0.5*(m_w*c2*1.79e-36)*(vo/100)*(vo/100))/(1.609e-19);

  // loop over energy recoil range in keV
  for (int j=1;j<101;j++)
  {
    // recoil energy in eV
    Double_t Er = histrate->GetBinCenter(j)*1000;                    //
    // form factor variables
    Double_t qr   = 6.92e-3*sqrt( A*Er/1000.)*(1.14*pow(A, 1.0/3.0) );
    Double_t qs   = 6.92e-3*sqrt( A*Er/1000.)*0.9;
    // Helm Form Factor
    Double_t F    = 3*(sin(qr)/(qr*qr*qr) - cos(qr)/(qr*qr))*exp(-qs*qs/2);
    // Minimum WIMP velocity, corresponding to minimum energy
```

```
54      Double_t vmin   = sqrt(Er/(Eo*r))*vo;
55      // Differential rate (keV^-1 kg^-1 day^-1)
56      Double_t dRdEr  = t*1000*pow(F,2)*(Ro/((Eo/1000)*r))*sqrt(pi)*vo/(4*ve)
            *(TMath::Erf( (vmin+ve)/vo) -TMath::Erf( (vmin-ve)/vo ) ) ;
57      histrate->SetBinContent(j, dRdEr);
58    }
59
60    //--------- plotting histogram
61    TCanvas * canvas = new TCanvas("canvas","canvas",200,10,1000,800);
62    canvas->SetLogy();
63    histrate->Draw("L");
64    histrate->GetXaxis()->SetTitle("Recoil energy (keV)");
65    histrate->GetYaxis()->SetTitle("dR/dEr (events keV^{-1} kg^{-1} year
          ^{-1})");
66    histrate->SetLineColor(kPink-9);
67    histrate->SetLineWidth(1);
68    histrate->SetMinimum(0.00005);
69    histrate->SetMaximum(0.005);
70
71    TAxis* xax = histrate->GetXaxis();
72    xax->CenterTitle(true);
73    xax->SetNdivisions(512);
74    xax->SetLabelFont(42);
75    xax->SetLabelOffset(0.012);
76    xax->SetLabelSize(0.03);
77    xax->SetTitleSize(0.035);
78    xax->SetTitleOffset(1.65);
79    xax->SetTitleFont(42);
80    TAxis* yax = histrate->GetYaxis();
81    yax->CenterTitle(true);
82    yax->SetNdivisions(512);
83    yax->SetLabelFont(42);
84    yax->SetTitleOffset(1.65);
85    yax->SetLabelSize(0.03);
86    yax->SetTitleSize(0.035);
87    yax->SetTitleFont(42);
88    yax->SetLabelOffset(0.012);
89    TPaveText *pt = new TPaveText(0.3,0.9,0.7,1.01,"NDC");
90    pt->AddText("WIMP-induced nuclear recoil energy spectrum");
91    pt->SetFillColor(0);
92    pt->SetLineColor(0);
93    pt->SetTextFont(52);
94    pt->SetTextSize(0.04);
95    pt->SetBorderSize(0);
96    pt->Draw();
97    TPaveText *pt2 = new TPaveText(0.1,0.92,0.9,0.92,"NDC");
98    pt2->AddText("(WIMP of mass 100GeVc^{-2} and cross section 10^{-45} cm
          ^{2})");
99    pt2->SetFillColor(0);
100   pt2->SetLineColor(0);
101   pt2->SetTextFont(52);
102   pt2->SetTextSize(0.02);
103   pt2->SetBorderSize(0);
104   pt2->Draw();
105
106   return;
107 }
```

6.4 Appendix D: DEAP-3600 sensitivity plot ROOT code

DEAP 3600 sensitivity plot of cross section vs mass (assuming 2.3 events in 3 years in a 1000kg fiducial mass). Generated in ROOT version: 5.34/10. Derivation follows J.D. Lewin, RF. Smith: Review of mathematics, numerical factors, and corrections for dark matter experiments based on elastic nuclear recoil. Detector response from dark2.C and QWimp macro by M. Boulay 2006-2012

```
1  #include "TH1.h"
2  #include "TObject.h"
3  #include "TF1.h"
4  #include "math.h"
5  #include "TMath.h"
6
7  void DEAPsensitivity()
8  {
9    //--------- clear objects from previous runs
10   delete gDirectory->FindObject("canvas");
11   delete gDirectory->FindObject("graph");
12   delete gDirectory->FindObject("recoil");
13   delete gDirectory->FindObject("teff");
14
15   //--------- histograms for calculations
16   // WIMP recoil energy distribution (keVr)
17   TH1F * recoil = new TH1F("recoil","",500,0,500);
18   // detector energy resolution function
19   TF1 * tres = new TF1("tres","pol2",0,1000);
20   // parameters for argon detector
21   tres->SetParameters(0.965,0.787,5.33e-3);
22   // response function
23   TF1 * tresponse = new TF1("tresponse","gaus");
24   // measured energy distribution (keVee)
25   TH1F * teff = new TH1F("teff","",500,0,500);
26
27   //--------- define all constants
28   Double_t Ethresh    = 15;        // energy threshold in keVee
29   Double_t Ewin       = 25;        // energy window in keVee
30   Double_t mDEAP      = 1000000;       // target mass in g
31   Double_t quench     = 0.25;        // recoil energy quenching factor
32   Double_t c          = 2.99792458e10;  // speed of light in cm/sec
33   Double_t c2         = c*c;         // speed of light squared
34   Double_t A          = 40;        // nuclear target atomic number (g/mol)
35   Double_t sigman     = 1e-42;       // WIMP-Nucleon cross-section (cm^2)
36   Double_t rho0       = 0.3e9/(c*c);     // WIMP density in eV/cm^3
37   Double_t vo         = 22000000.;     // WIMP wind velocity in cm/sec
38   Double_t ve         = 24400000.;     // Earth velocity in cm/sec
39   Double_t t          = 86400*365.25*3; // 3 year experiment in seconds
40   Double_t pi         = TMath::Pi();     // pi
41   Double_t m_N        = A*931.5e6/c2;    // Nucleus mass in eV
42   Double_t m_n        = 931.5*1e6/c2;      // Nucleon mass in eV
43   Double_t avogadro   = 6.0221413e+23;  // Avogadro's constant
44
45   //--------- main variable vectors for plot and loop index
46   Double_t wimpmass[1000];
47   Double_t wimpcsc[1000];
48   Int_t n = 0;
49
```

```
50    // - - - - - - - - for loop over mass range
51
52      // loop over log of the masses i.e. 0 to about 16000GeV/c^2
53      for (Double_t i=0; i<=4.2; i+=0.1)
54      {
55        // WIMP mass in GeV/c^2
56        wimpmass[n]    = pow(10,i);
57        // WIMP mass in eV
58        Double_t m_w  = pow(10,i)*1e9/c2;
59        //WIMP-nucleus cross-section, spin-independant
60        Double_t sigma0 = A*A*sigman*pow(((m_N*m_w)/(m_N+m_w))/((m_n*m_w)/(
              m_n+m_w)),2);
61        // Event rate/mass/time (g^-1 s^-1)
62        Double_t Ro    = 2*avogadro*rho0*sigma0*vo/(sqrt(pi)*A*m_w);
63        // Kinematic factor (unitless)
64        Double_t r     = 4*m_N*m_w/pow((m_N+m_w),2);
65        // Average WIMP energy in eV
66        Double_t Eo    = (0.5*(m_w*c2*1.79e-36)*(vo/100)*(vo/100))/(1.609e-19)
              ;
67
68        // - - - - - - - - for loop to calculate the total rate for each mass
69
70        teff->Reset();  //reset for each mass loop
71
72        // loop over energy recoil range in keV
73        for(Int_t j=1; j<=500; j++)
74        {
75          // recoil energy in eV
76          Double_t Er    = recoil->GetBinCenter(j)*1000;
77          // form factor variables
78          Double_t qr    = 6.92e-3*sqrt( A*Er/1000.)*(1.14*pow(A, 1.0/3.0) );
79          Double_t qs    = 6.92e-3*sqrt( A*Er/1000.)*0.9;
80          // Helm Form Factor
81          Double_t F     = 3*(sin(qr)/(qr*qr*qr) - cos(qr)/(qr*qr))*exp(-qs*qs
                /2);
82          // Minimum WIMP velocity, corresponding to minimum energy
83          Double_t vmin    = sqrt(Er/(Eo*r))*vo;
84          // Differential rate (keV^-1 g^-1 s^-1)
85          Double_t dRdEr  = pow(F,2)*(Ro/((Eo/1000)*r))*sqrt(pi)*vo/(4*ve)*(
                TMath::Erf( (vmin+ve)/vo) -TMath::Erf( (vmin-ve)/vo ) ) ;
86          // Differential rate for DEAP-3600 - multiply by target mass and
                exposure time  (keV^-1)
87          recoil->SetBinContent(j, dRdEr*t*mDEAP);
88
89          // - - - - - - - - - detector energy resolution correction
90          Double_t tsigma = tres->Eval( sqrt( Er*quench/1000. ) );
91          tresponse->SetParameters(1, Er*quench/1000., tsigma );
92          tresponse->SetParameter(0, tresponse->GetParameter(0)/tresponse->
                Integral( Er*quench/1000.-5*tsigma, Er*quench/1000.+5*tsigma )
                );
93          tresponse->SetRange(Er*quench/1000.-7*tsigma, Er*quench/1000.+7*
                tsigma );
94
95          for(Int_t k=1; k<=500; k++)
96          {
97            teff->AddBinContent(k, recoil->GetBinContent(j)*tresponse->Eval(
                  teff->GetBinCenter(k) ) );
98          }
99        }
```

```
100
101         // ---------- rate as integral over energy plot
102         Int_t binlo = teff->GetXaxis()->FindBin(Ethresh);
103         Int_t binhi = teff->GetXaxis()->FindBin(Ethresh+Ewin);
104         Double_t rate = teff->Integral(binlo, binhi);
105         // 10% probability to see 0 events for mean=2.3
106         wimpcsc[n] = 2.3*sigman/rate;
107         n++;
108       }
109
110       // --------- plot the results
111       TCanvas *canvas = new TCanvas("canvas","DEAP-3600 sensitivity"
              ,200,10,1000,800);
112       canvas->SetLogy();
113       canvas->SetLogx();
114       graph = new TGraph(n, wimpmass, wimpcsc);
115       graph->Draw("AL");
116       graph->SetMinimum(1e-48);
117       graph->SetMaximum(1e-40);
118       graph->GetXaxis()->SetLimits(8, 10000);
119       graph->GetXaxis()->SetTitle("m_{w} (GeV)");
120       graph->GetXaxis()->SetLabelSize(0.03);
121       graph->GetXaxis()->SetLabelOffset(0.012);
122       graph->GetXaxis()->SetTitleSize(0.035);
123       graph->GetXaxis()->SetTitleOffset(1.65);
124       graph->GetXaxis()->SetTickLength(0.02);
125       graph->GetYaxis()->SetTitle("#sigma (cm^{2})");
126       graph->GetYaxis()->SetLabelSize(0.03);
127       graph->GetYaxis()->SetLabelOffset(0.012);
128       graph->GetYaxis()->SetTitleSize(0.035);
129       graph->GetYaxis()->SetTitleOffset(1.65);
130       graph->GetYaxis()->SetTickLength(0.01);
131       graph->SetLineColor(kPink-9);
132       graph->SetLineWidth(1);
133
134       // --------- Create text box to generate customised title box
135       TPaveText *pt = new TPaveText(0.18,0.9,0.9,1.03,"NDC");
136       pt->AddText("DEAP-3600 sensitivity");
137       pt->SetFillColor(0);
138       pt->SetLineColor(0);
139       pt->SetTextFont(52);
140       pt->SetTextSize(0.05);
141       pt->SetBorderSize(0);
142       pt->Draw();
143       TPaveText *pt2 = new TPaveText(0.18,0.93,0.9,0.92,"NDC");
144       pt2->AddText("(Assuming 2.3 events in 3 years in a 1000kg fiducial mass
              )");
145       pt2->SetFillColor(0);
146       pt2->SetLineColor(0);
147       pt2->SetTextFont(52);
148       pt2->SetTextSize(0.025);
149       pt2->SetBorderSize(0);
150       pt2->Draw();
151
152       return;
153     }
```